COMMUNICATIONS IN COMPUTATIONAL PHYSICS
Vol. **2**, No. 5, pp. 827-880

Commun. Comput. Phys.
October 2007

REVIEW ARTICLE

Mathematical Models and Numerical Methods for High Frequency Waves

Olof Runborg*

Department of Numerical Analysis, School of Computer Science and Communication, KTH, 100 44 Stockholm, Sweden.

Received 3 December 2006; Accepted (in revised version) 26 January 27

Communicated by Weinan E

Available online 20 March 2007

Abstract. The numerical approximation of high frequency wave propagation is important in many applications. Examples include the simulation of seismic, acoustic, optical waves and microwaves. When the frequency of the waves is high, this is a difficult multiscale problem. The wavelength is short compared to the overall size of the computational domain and direct simulation using the standard wave equations is very expensive. Fortunately, there are computationally much less costly models, that are good approximations of many wave equations precisely for very high frequencies. Even for linear wave equations these models are often nonlinear. The goal of this paper is to review such mathematical models for high frequency waves, and to survey numerical methods used in simulations. We focus on the geometrical optics approximation which describes the infinite frequency limit of wave equations. We will also discuss finite frequency corrections and some other models.

AMS subject classfications: 65-02, 35L05, 78A05

Key words: Geometrical optics, wave equation, Helmholtz equation, high frequency waves, eikonal equation, ray tracing, multiscale problems.

Contents

*Corresponding author. *Email address:* olofr@nada.kth.se (O. Runborg)

1 Introduction

In this review we consider numerical simulation of waves at high frequencies, and the underlying mathematical models used. For simplicity we will mainly discuss the linear scalar wave equation,

$$u_{tt} - c(\boldsymbol{x})^2 \Delta u = 0, \qquad (t,\boldsymbol{x}) \in \mathbb{R}^+ \times \Omega, \qquad \Omega \subset \mathbb{R}^d, \tag{1.1}$$

where $c(\boldsymbol{x})$ is the local speed of wave propagation of the medium. We complement (1.1) with initial or boundary data that generate high-frequency solutions. The exact form of the data will not be important here, but a typical example would be $u(0,\boldsymbol{x}) = A(\boldsymbol{x})\exp(i\omega \boldsymbol{k}\cdot\boldsymbol{x})$ where $|\boldsymbol{k}| = 1$ and the frequency $\omega \gg 1$. With slight modifications, the techniques we describe will also carry over to systems of wave equations, like the Maxwell equations and the elastic wave equation.

When the frequency of the waves is high, (1.1) is a multiscale problem, where the small scale is given by the wavelength, and the large scale corresponds to the overall size of the computational domain. In the direct numerical simulation of (1.1) the accuracy of the solution is determined by the number of grid points or elements per wavelength. The computational cost to maintain constant accuracy grows algebraically with the frequency, and for sufficiently high frequencies, direct numerical simulation is no longer feasible. Numerical methods based on approximations of (1.1) are needed.

Let us mention before continuing that this multiscale problem is prevalent in many applications for different types of waves: elastic, electromagnetic as well as acoustic. Seismic wave propagation, for instance, is a challenging elastic wave problem. Both the forward and the inverse problems are of great interest and high frequency approximations must be used when the relative wavelength is short. In computational electromagnetics (CEM) radiation and scattering problems, such as radar cross section (RCS) computations, are important. Electromagnetic waves emitted by communication or radar devices often have a very small wavelength compared to the size of the scatterer, which can be an entire aircraft. For acoustic problems high frequency techniques become interesting, for instance, in underwater acoustics where waves of moderate frequency travel over very large distances.

Fortunately, there exist good approximations of many wave equations precisely for very high frequency solutions. In this paper we mainly consider variants of *geometrical optics*, which are asymptotic approximations obtained when the frequency tends to infinity. These approximations are widely used in applications. Instead of the oscillating wave field the unknowns in standard geometrical optics are the phase and the amplitude, which typically vary on a much coarser scale than the full solution. Hence, they should in principle be easier to compute numerically.

Geometrical optics can be formulated in several different ways. Assuming the solution can be approximated by a simple wave,

$$u(t,\boldsymbol{x}) \approx A(t,\boldsymbol{x})e^{i\omega\phi(t,\boldsymbol{x})}, \tag{1.2}$$

one classical formulation is the partial differential equations (PDEs) for ϕ and A. The phase function ϕ satisfies the Hamilton–Jacobi-type *eikonal equation*,

$$\phi_t + c(\boldsymbol{x})|\nabla\phi| = 0, \tag{1.3}$$

where $|\cdot|$ denotes the Euclidean norm in $\mathbb{R}^d$. For the leading order amplitude term A one obtains the *transport equation*

$$A_t + c(\boldsymbol{x})\frac{\nabla\phi\cdot\nabla A}{|\nabla\phi|} + \frac{c(\boldsymbol{x})^2\Delta\phi - \phi_{tt}}{2c(\boldsymbol{x})|\nabla\phi|}A = 0. \tag{1.4}$$

Geometrical optics can also be formulated in terms of *ray tracing*. This is an ordinary differential equation (ODE) model. As long as the phase function is smooth, it corresponds to solving the eikonal equation (1.3) through the method of characteristics, *i.e.* solving the system of ODEs,

$$\frac{d\boldsymbol{x}}{dt} = \nabla_p H(\boldsymbol{x},\boldsymbol{p}), \qquad \frac{d\boldsymbol{p}}{dt} = -\nabla_x H(\boldsymbol{x},\boldsymbol{p}), \qquad H(\boldsymbol{x},\boldsymbol{p}) = c(\boldsymbol{x})|\boldsymbol{p}|, \tag{1.5}$$

where the momentum variable $\boldsymbol{p}\in\mathbb{R}^d$ is usually called the *slowness* vector. There are also ODEs to compute the amplitude A.

Finally, there is a "kinetic" formulation, which have proved to be a useful basis for some new numerical techniques. The kinetic model is based on the interpretation that rays are trajectories of particles following Hamiltonian dynamics. In the phase space $(t,\boldsymbol{x},\boldsymbol{p})$ the evolution of a particle is governed by (1.5). Letting $f(t,\boldsymbol{x},\boldsymbol{p})$ be a particle density function, it will then satisfy the Liouville equation,

$$f_t + \nabla_p H\cdot\nabla_x f - \nabla_x H\cdot\nabla_p f = 0. \tag{1.6}$$

The main drawbacks of the infinite frequency approximation of geometrical optics are that diffraction effects at boundaries are lost, and that the approximation breaks down at caustics, where the predicted amplitude A is unbounded. For these situations more detailed models are needed, such as the *geometrical theory of diffraction* (GTD) [52], which adds diffraction phenomena by explicitly taking into account the geometry of Ω and boundary conditions. The solution's asymptotic behavior close to caustics can also be derived, and a correct amplitude for finite frequency can be computed [25, 42, 56, 66, 67].

High frequency wave propagation is thus well approximated by asymptotic formulations like geometrical optics and the geometrical theory of diffraction. These formulations can be used analytically for the understanding of high frequency phenomena but also as the basis for computations. The ray tracing equations (1.5) can be solved directly with numerical methods for ODEs. This gives the phase and amplitude solution along a ray, and interpolation must be applied to obtain those quantities everywhere. The interpolation can be simplified by instead using so-called wave front methods. They are related to ray tracing, but instead of individual rays, an interface representing a wave

front is evolved according to the ray equations. The eikonal and transport equations (1.3, 1.4) can also be solved with numerical PDE methods on regular grids. However, this only gives the correct solution when it is a single wave of the form (1.2). When there are crossing waves, more elaborate schemes must be devised. Methods using the kinetic formulation can be seen as a compromise between ray tracing and eikonal equation methods. The Liouville equation (1.6) accepts crossing wave solutions and can in principle be solved as a PDE. The computational drawback of (1.6) is the large number of independent variables, a consequence of its being set in the full phase space. Unless solutions for many different sources is of interest, the computational complexity of solving (1.6) is far from competitive compared to the other methods. The complexity can be reduced, however. This is done in moment methods by considering the equations for the moments of the density function f, set in $(t,\boldsymbol{x})$-space, and using the closure assumption that there are only a fixed, finite, number of crossing waves at each point.

The purpose of this paper is to review the mathematical models and numerical methods outlined above. For other reviews of this topic, see [10, 27, 65]. The paper is organized as follows. After this introductory section, there are two main parts. In Section 2 the mathematical models discussed above, as well as some additional ones, are derived and explained in more detail. This is followed by Section 3, where a survey of numerical methods for the high frequency models is given.

2 Mathematical background

In this chapter we derive the equations that are used in geometrical optics. We also discuss corrections to the standard geometrical optics approximation and some other high frequency models.

The starting point is the Cauchy problem for the scalar wave equation (1.1),

$$\begin{aligned} &u_{tt}(\boldsymbol{x},t)-c(\boldsymbol{x})^2\Delta u(\boldsymbol{x},t)=0, && \boldsymbol{x}\in\mathbb{R}^d,\ t>0,\\ &u(\boldsymbol{x},0)=u_0(\boldsymbol{x}), && \boldsymbol{x}\in\mathbb{R}^d,\\ &u_t(\boldsymbol{x},0)=u_1(\boldsymbol{x}), && \boldsymbol{x}\in\mathbb{R}^d, \end{aligned} \tag{2.1}$$

with highly oscillatory initial data u_0 and u_1. Here $c(\boldsymbol{x})$ is the local wave velocity of the medium. We also define the *index of refraction* as $\eta(\boldsymbol{x})=c_0/c(\boldsymbol{x})$ with the reference velocity c_0 (*e.g.* the speed of light in vacuum). For simplicity we will henceforth let $c_0=1$. When c is constant (2.1) admits the simple plane wave solution

$$u(t,\boldsymbol{x})=Ae^{i\omega(ct-\boldsymbol{k}\cdot\boldsymbol{x})}, \qquad |\boldsymbol{k}|=1, \tag{2.2}$$

where ω is the frequency, $\boldsymbol{k}$ is the wave vector giving the direction of propagation and A is a constant representing the amplitude. The parameters ω, $\boldsymbol{k}$ and A are determined by appropriate initial data. For more complicated waves and when c is not constant, we

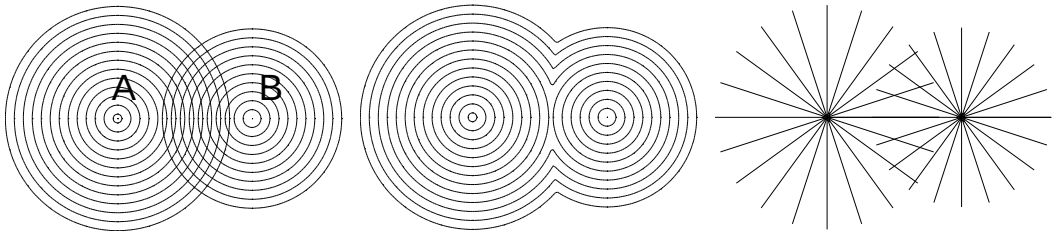

(a) Correct solution (b) Eikonal equation (c) Ray tracing

Figure 1: Solution after some time to a homogeneous problem with two point sources, A and B, where the A source began transmitting slightly before the B source. The left figure shows the physically correct solution with two superimposed wave fields. Level curves of their phase functions are plotted. The middle figure shows level curves of ϕ in the viscosity solution of the eikonal equation (2.6). Note that the superposition principle does not hold. Instead, the first arriving wave takes precedence over the second at each point. The right figure shows a ray-traced solution

need to replace $ct-\boldsymbol{k}\cdot\boldsymbol{x}$ by a general *phase function* $\phi(t,\boldsymbol{x})$, and also permit the amplitude to depend on time, space and frequency. Hence, (2.1) has solutions of the type

$$u(t,\boldsymbol{x}) = A(t,\boldsymbol{x},\omega)e^{i\omega\phi(t,\boldsymbol{x})}. \tag{2.3}$$

The level curves of ϕ corresponds to the wave fronts of a propagating wave: *cf.* Fig. 1.

Since (2.1) is linear, the superposition principle is valid and a sum of solutions is itself a solution (provided initial data is adapted accordingly). The generic solution to (2.1) is, at least locally, described by a finite sum of terms like (2.3),

$$u(t,\boldsymbol{x}) = \sum_{n=1}^{N} A_n(t,\boldsymbol{x},\omega)e^{i\omega\phi_n(t,\boldsymbol{x})}. \tag{2.4}$$

with A_n, ϕ_n being smooth functions and A_n depending only mildly on the frequency ω. Typically this setting only breaks down at a small set of points, namely focus points, caustics, discontinuities in $c(\boldsymbol{x})$ and non-smooth boundary points.

We will first assume the validity of the geometrical optics approximation that $\omega\to\infty$. This means that we accept the loss of diffraction phenomena in the solution due to non-smooth boundaries and $c(\boldsymbol{x})$, as well as the break down of the wave amplitude approximation at caustics. There are three strongly related formulations of geometrical optics, which we will review in Section 2.1 to Section 2.3. The derivation of the geometrical optics equations in this linear case is classical: see, for instance, the book by Whitham, [106]. For a rigorous treatment of propagation of singularities in linear partial differential equations, we refer to the books by Hörmander, [42]. After discussing boundary and interface conditions in Section 2.4, we shall comment in Section 2.5 on a few techniques to correct the standard geometrical optics approximation at caustics and to add diffraction effects. Finally we consider two other high frequency models in Section 2.6: the physical optics approximation and gaussian wave packets. These models handle high frequencies more efficiently than direct numerical approximation of the wave equation (2.1), and they include some phenomena that are not described by geometrical optics.

2.1 Eikonal equation

Let us now derive Eulerian PDEs for the phase and the amplitude functions that are formally valid in the limit when $\omega\to\infty$. Our focus on these functions is motivated by the observation that the phase and amplitude in (2.3) generically vary on a much larger scale than the solution u itself, and should therefore be easier to compute. In the homogeneous case (2.2), for instance, $\phi=ct-\boldsymbol{k}\cdot\boldsymbol{x}$ stays nonoscillating and bounded independently of ω.

To begin with we assume that the solution to (2.1) has the form (2.3) and that the amplitude function in (2.3) can be expanded in a power series in $1/i\omega$. We then get the asymptotic WKB expansion, [42],

$$u=e^{i\omega\phi(t,\boldsymbol{x})}\sum_{k=0}^{\infty}a_k(t,\boldsymbol{x})(i\omega)^{-k}. \tag{2.5}$$

We substitute this expression into (2.1), and equate coefficients of powers of ω to zero. For ω^2, this gives the *eikonal equation*,

$$\phi_t\pm c|\nabla\phi|=0. \tag{2.6}$$

In fact, because of the sign ambiguity we get two eikonal equations. Without loss of generality we will henceforth consider the one with a plus sign. For ω^1, we get the *transport equation* for the first amplitude term,

$$(a_0)_t+c\frac{\nabla\phi\cdot\nabla a_0}{|\nabla\phi|}+\frac{c^2\Delta\phi-\phi_{tt}}{2c|\nabla\phi|}a_0=0. \tag{2.7}$$

For higher-order terms of $1/i\omega$, we get additional transport equations

$$(a_{k+1})_t+c\frac{\nabla\phi\cdot\nabla a_{k+1}}{|\nabla\phi|}+\frac{c^2\Delta\phi-\phi_{tt}}{2c|\nabla\phi|}a_{k+1}+\frac{c^2\Delta a_k-(a_k)_{tt}}{2c|\nabla\phi|}=0 \tag{2.8}$$

for the remaining amplitude terms. When ω is large, only the first term in the expansion (2.5) is significant, and the problem is reduced to computing the phase ϕ and the first amplitude term a_0. Note that, once ϕ is known, the transport equations are linear equations with variable coefficients.

Instead of the time-dependent wave equation (2.1) we can consider the frequency domain problem. Setting $u(t,\boldsymbol{x})=v(\boldsymbol{x})\exp(i\omega t)$ with ω fixed, v satisfies the Helmholtz equation

$$c^2\Delta v+\omega^2 v=0. \tag{2.9}$$

Substituting the series

$$v=e^{i\omega\tilde{\phi}(\boldsymbol{x})}\sum_{k=0}^{\infty}\tilde{a}_k(\boldsymbol{x})(i\omega)^{-k} \tag{2.10}$$

into (2.9), we get an alternative, frequency domain, version of the pair (2.6, 2.7),

$$|\nabla\tilde{\phi}|=1/c=\eta,\qquad 2\nabla\tilde{\phi}\cdot\nabla\tilde{a}_0+\Delta\tilde{\phi}\tilde{a}_0=0. \tag{2.11}$$

With consistent initial and boundary data, $\phi(t,\boldsymbol{x})=\tilde{\phi}(\boldsymbol{x})-t$. We note that, since the family of curves $\{\boldsymbol{x}|\phi(t,\boldsymbol{x})=\tilde{\phi}(\boldsymbol{x})-t=0\}$, parametrized by $t\geq 0$, describe a propagating wave front in (2.5), we often directly interpret the frequency domain phase $\tilde{\phi}(\boldsymbol{x})$ as the *travel time* of a wave. The difference in phase between two points on the same characteristic signifies the time it takes for a wave to travel between them.

In what follows we will denote the first amplitude term a_0 by A (or A_1, A_2, etc. when there are multiple crossing waves). We also drop the tilde for the frequency domain quantities.

One problem with the eikonal and transport equations is that they do not accept solutions with multiple phases. There is no superposition principle for the nonlinear eikonal equation: *cf.* Fig. 1. A finite sum of solutions of the form (2.4), with slowly varying A_n and ϕ_n, can in general not be well approximated by the first term in the ansatz (2.5) at high frequencies. In fact, for the case in (2.4), the derivation must be done term wise, and the $\{\phi_n\}$ and $\{A_n\}$ will, locally, satisfy separate eikonal and transport equation pairs.

However, the eikonal equation still has a well-defined solution. It is a nonlinear Hamilton–Jacobi-type equation with Hamiltonian $H(\boldsymbol{x},\boldsymbol{p})=c(\boldsymbol{x})|\boldsymbol{p}|$. As in the case of hyperbolic conservation laws, extra conditions are needed for this type of equations to have a unique solution. These were given in [23] and the solution is known as the *viscosity solution*, which is the analogue of the entropy solution for conservation laws. As can be deduced from the previous paragraph, the viscosity solution does not have to agree with the correct physical solution in all cases. At points where the correct solution should have a multivalued phase, *i.e.* be of the type in (2.4), the viscosity solution picks out the phase corresponding to the first arriving wave, *i.e.* the smallest ϕ_n in (2.4).

It is well known that solutions of Hamilton–Jacobi-equations can develop kinks, *i.e.* discontinuities in the gradient, just as shocks appear in the solutions of conservation laws. In the case of the eikonal equation, the kinks are located where the physically correct phase solution should become multivalued: *cf.* Fig. 1. We notice that the transport equation (2.7) has a factor involving $\Delta\phi$, which is not bounded at kinks, and therefore we can expect blow-up of a_0 at these points.

2.2 Ray equations

Another formulation of geometrical optics is *ray tracing*, which gives the solution via ODEs. This Lagrangian formulation is closely related to the method of characteristics for (2.6). Let $(\boldsymbol{x}(t),\boldsymbol{p}(t))$ be a bicharacteristic pair related to the Hamiltonian $H(\boldsymbol{x},\boldsymbol{p})=c(\boldsymbol{x})|\boldsymbol{p}|$, hence

$$\frac{d\boldsymbol{x}}{dt}=\nabla_p H(\boldsymbol{x},\boldsymbol{p})=c(\boldsymbol{x})\frac{\boldsymbol{p}}{|\boldsymbol{p}|},\qquad \boldsymbol{x}(0)=\boldsymbol{x}_0, \tag{2.12}$$

$$\frac{d\boldsymbol{p}}{dt}=-\nabla_x H(\boldsymbol{x},\boldsymbol{p})=-|\boldsymbol{p}|\nabla c(\boldsymbol{x}),\quad \boldsymbol{p}(0)=\boldsymbol{p}_0. \tag{2.13}$$

In d dimensions the bicharacteristics are curves in $2d$-dimensional *phase space*, $(\boldsymbol{x},\boldsymbol{p})\in\mathbb{R}^{d\times d}$. It follows immediately that H is constant along them, $H(\boldsymbol{x}(t),\boldsymbol{p}(t))=H(\boldsymbol{x}_0,\boldsymbol{p}_0)$. We

are interested in solutions for which $H\equiv 1$. In this case the projections on physical space, $\boldsymbol{x}(t)$, are usually called *rays*, and we can reduce (2.12, 2.13) to

$$\frac{d\boldsymbol{x}}{dt}=\frac{1}{\eta^2}\boldsymbol{p}, \qquad \boldsymbol{x}(0)=\boldsymbol{x}_0, \tag{2.14}$$

$$\frac{d\boldsymbol{p}}{dt}=\frac{\nabla\eta}{\eta}, \qquad \boldsymbol{p}(0)=\boldsymbol{p}_0, \quad |\boldsymbol{p}_0|=\eta(\boldsymbol{x}_0). \tag{2.15}$$

Solving (2.14, 2.15) is called *ray tracing*. It should be noted here that if $\eta=$const the rays are just straight lines.

We use the frequency domain version of the eikonal equation, (2.11), to explain the significance of the bicharacteristics when the solution ϕ is smooth. It can be written as

$$H(\boldsymbol{x},\nabla\phi(\boldsymbol{x}))=1, \tag{2.16}$$

with H as above. By differentiating (2.16) with respect to $\boldsymbol{x}$, we get

$$\nabla_x H(\boldsymbol{x},\nabla\phi(\boldsymbol{x}))+D^2\phi(\boldsymbol{x})\nabla_p H(\boldsymbol{x},\nabla\phi(\boldsymbol{x}))=0.$$

Here, D^2 represents the Hessian. Then, for any curve $\boldsymbol{y}(t)$ we have the identity

$$\begin{aligned}&\frac{d}{dt}\nabla\phi(\boldsymbol{y}(t))=D^2\phi(\boldsymbol{y}(t))\frac{d\boldsymbol{y}(t)}{dt}\\ &=D^2\phi(\boldsymbol{y}(t))\left[\frac{d\boldsymbol{y}(t)}{dt}-\nabla_p H(\boldsymbol{y}(t),\nabla\phi(\boldsymbol{y}(t)))\right]-\nabla_x H(\boldsymbol{y},\nabla\phi(\boldsymbol{y}(t))).\end{aligned} \tag{2.17}$$

Taking $\boldsymbol{x}(t)$ to be the curve for which the expression in brackets vanishes, we see that $(\boldsymbol{x}(t),\nabla\phi(\boldsymbol{x}(t)))$ is a bicharacteristic. By the uniqueness of solutions to (2.12, 2.13), we therefore have that $\boldsymbol{p}(t)\equiv\nabla\phi(\boldsymbol{x}(t))$ if we take $\boldsymbol{p}_0=\nabla\phi(\boldsymbol{x}_0)$. Hence, with this initialization, the rays are always orthogonal to the level curves of ϕ, since $d\boldsymbol{x}/dt$ is parallel to $\boldsymbol{p}=\nabla\phi$ by (2.14). Moreover, for our particular H,

$$\frac{d}{dt}\phi(\boldsymbol{x}(t))=\nabla\phi(\boldsymbol{x}(t))\cdot\frac{d\boldsymbol{x}(t)}{dt}=\boldsymbol{p}(t)\cdot\nabla_p H(\boldsymbol{x}(t),\boldsymbol{p}(t))=H(\boldsymbol{x}(t), \quad \boldsymbol{p}(t))=1. \tag{2.18}$$

Thus, as long as ϕ is smooth, the solution to (2.16) along the ray is given by the simple expression

$$\phi(\boldsymbol{x}(t))=\phi(\boldsymbol{x}_0)+t. \tag{2.19}$$

Since ϕ corresponds to travel time, this also verifies that the parametrization t in (2.12, 2.13) indeed corresponds to unscaled time; the ray $\boldsymbol{x}(t)$ traces one point on a propagating wave front at time t. The absolute value of its time derivative $|d\boldsymbol{x}/dt|$ is precisely the local speed of propagation $c(\boldsymbol{x})$ by (2.14), and since $\boldsymbol{p}$ is parallel to $d\boldsymbol{x}/dt$, while $|\boldsymbol{p}|=H(\boldsymbol{x},\boldsymbol{p})c(\boldsymbol{x})^{-1}=c(\boldsymbol{x})^{-1}$ by (2.16), the vector $\boldsymbol{p}$ is often called the *slowness* vector.

As was discussed in Section 2.1, the solution of the eikonal equation (2.6) is valid up to the point where discontinuities appear in the gradient of ϕ. This is where the

phase should become multivalued but, by the construction, cannot. The bicharacteristics, however, do not have this problem, and we can extend their validity to all t, see Fig. 1.

The rays can also be derived from the calculus of variations, using Fermat's principle. By analogy with the least action principle in classical mechanics, it says that the rays between two points are stationary curves of the functional

$$I[\gamma] = \int_\gamma \eta(\boldsymbol{x}) d\boldsymbol{x},$$

taken over all curves γ starting and ending at the points in question. The Euler–Lagrange equations for this optimization problem give the same bicharacteristics as (2.12, 2.13), but the formulation is also well defined for non-differentiable η. The integral represents the length of γ under the measure ηds and therefore we often describe the rays as the *shortest optical path* between two points.

In order to compute the amplitude along a ray we also need information about the local shape of the ray's source. Let $(\boldsymbol{x}(t,\boldsymbol{x}_0),\boldsymbol{p}(t,\boldsymbol{x}_0))$ denote the bicharacteristic originating in $\boldsymbol{x}_0$ with $\boldsymbol{p}(0,\boldsymbol{x}_0) = \nabla\phi(\boldsymbol{x}_0)$, hence $\boldsymbol{x}(0,\boldsymbol{x}_0) = \boldsymbol{x}_0$. Let $J(t,\boldsymbol{x}_0)$ be the Jacobian of $\boldsymbol{x}$ with respect to initial data, $J = D_{x_0}\boldsymbol{x}(t,\boldsymbol{x}_0)$. By differentiating (2.14) we get

$$\begin{aligned}\frac{\partial J}{\partial t} &= D_{x_0}\frac{\partial \boldsymbol{x}(t,\boldsymbol{x}_0)}{\partial t} = D_{x_0} c(\boldsymbol{x}(t,\boldsymbol{x}_0))^2 \boldsymbol{p}(t,\boldsymbol{x}_0)\\ &= D_{x_0} c^2(\boldsymbol{x}(t,\boldsymbol{x}_0))\nabla\phi(\boldsymbol{x}(t,\boldsymbol{x}_0)) = \left(D_{x_0} c^2 \nabla\phi\right) J.\end{aligned}$$

Assume that J is nonsingular and let $J = S\Lambda S^{-1}$ be a Jordan decomposition, so that the diagonal entries of Λ are the eigenvalues $\{\lambda_j\}$ of J. Setting $q = \det J = \prod_j \lambda_j$, and using the fact that $\mathrm{tr}(T^{-1}AT) = \mathrm{tr}A$, we have

$$\begin{aligned}&\frac{\partial q}{\partial t} = q\,\mathrm{tr}\left(\Lambda^{-1}\Lambda_t\right)\\ &= q\,\mathrm{tr}\left(S\Lambda^{-1}S^{-1}S\Lambda_t S^{-1} + (S\Lambda^{-1})S^{-1}S_t(S\Lambda^{-1})^{-1} + (S^{-1})_t S\right)\\ &= q\,\mathrm{tr}\left(J^{-1}J_t\right) = q\,\mathrm{tr}\left(J^{-1}\left(Dc^2\nabla\phi\right)J\right) = q\,\mathrm{tr}\left(Dc^2\nabla\phi\right) = q\nabla\cdot c^2\nabla\phi.\end{aligned}$$

Therefore differentiation along the ray gives

$$\begin{aligned}&\frac{d}{dt}\left[A^2(\boldsymbol{x}(t,\boldsymbol{x}_0))\eta(\boldsymbol{x}(t,\boldsymbol{x}_0))^2 q(t,\boldsymbol{x}_0)\right] = q(\nabla A^2\eta^2)\cdot\frac{\partial \boldsymbol{x}}{\partial t} + qA^2\eta^2\nabla\cdot c^2\nabla\phi\\ &= q\nabla\cdot(A^2\nabla\phi) = qA\left[2\nabla A\cdot\nabla\phi + \Delta\phi A\right] = 0,\end{aligned}$$

using (2.11) in the last step. It follows that the amplitude is given by the expression

$$A(\boldsymbol{x}(t,\boldsymbol{x}_0)) = A(\boldsymbol{x}_0)\frac{\eta(\boldsymbol{x}_0)}{\eta(\boldsymbol{x}(t,\boldsymbol{x}_0))}\sqrt{\frac{q(0,\boldsymbol{x}_0)}{q(t,\boldsymbol{x}_0)}}. \tag{2.20}$$

For example, an outgoing spherical wave centered at $\boldsymbol{x}=0$ in homogeneous medium with $\eta\equiv 1$ is given by $\boldsymbol{x}(t,\boldsymbol{x}_0)=\boldsymbol{x}_0+t\boldsymbol{x}_0/|\boldsymbol{x}_0|$. Then $J=I+t(I/|\boldsymbol{x}_0|-\boldsymbol{x}_0\boldsymbol{x}_0^T/|\boldsymbol{x}_0|^3)$ and $q=\det J=(1+t/|\boldsymbol{x}_0|)^{d-1}=(|\boldsymbol{x}|/|\boldsymbol{x}_0|)^{d-1}$ in d dimensions. Consequently, by (2.20), we get the well-known amplitude decay of such waves, $A\sim|\boldsymbol{x}|^{-(d-1)/2}$.

In order to compute A we thus need q, the determinant of $D_{x_0}\boldsymbol{x}$. The elements of this matrix is given by another ODE system. After differentiating (2.12, 2.13) with respect to $\boldsymbol{x}_0$, we obtain

$$\frac{d}{dt}\begin{pmatrix}D_{x_0}\boldsymbol{x}\\ D_{x_0}\boldsymbol{p}\end{pmatrix}=\begin{pmatrix}D^2_{px}H & D^2_{pp}H\\ -D^2_{xx}H & -(D^2_{px}H)^T\end{pmatrix}\begin{pmatrix}D_{x_0}\boldsymbol{x}\\ D_{x_0}\boldsymbol{p}\end{pmatrix}, \tag{2.21}$$

with initial data

$$D_{x_0}\boldsymbol{x}(0,\boldsymbol{x}_0)=I,\qquad D_{x_0}\boldsymbol{p}(0,\boldsymbol{x}_0)=D^2\phi(\boldsymbol{x}_0).$$

We note that the system matrix here only depends on $\boldsymbol{x}$ and $\boldsymbol{p}$.

The determinant q is often called the *geometrical spreading*, since it measures the size change of an infinitesimal area transported by the rays. Sets of points where $q=0$ are called *caustics*. These are points where rays concentrate, *cf.* Fig. 5. We see clearly from (2.20) that the amplitude is unbounded close to these points. In fact, we have only shown (2.20) as long as the ray does not encounter a caustic. Then J is nonsingular, and by continuity, $q(0)$ and $q(t)$ have the same sign. However, with a slight modification, the expression is also valid after caustic points, [67]. A careful analysis of the asymptotic behavior of the solution close to caustics reveals that

$$A(\boldsymbol{x}(t,\boldsymbol{x}_0))=A(\boldsymbol{x}_0)\frac{\eta(\boldsymbol{x}_0)}{\eta(\boldsymbol{x}(t,\boldsymbol{x}_0))}\sqrt{\left|\frac{q(0,\boldsymbol{x}_0)}{q(t,\boldsymbol{x}_0)}\right|}e^{-im\frac{\pi}{2}}, \tag{2.22}$$

where $m=m(t)$ is a nonnegative integer called the *Keller–Maslov index*. It represents the number of times $q(\cdot,\boldsymbol{x}_0)$ has changed sign in the interval $[0,t]$, *i.e.* the number of times that the ray has touched a caustic. Usually one counts the factor $\exp(-im\pi/2)$ as a phase shift of $m\pi/2\omega$ and subtract this from the eikonal ϕ, keeping A real.

The formation of caustics is related to the shape of the manifold

$$\Lambda=\Big\{(\boldsymbol{x}(t,\boldsymbol{x}_0),\boldsymbol{p}(t,\boldsymbol{x}_0))\in\mathbb{R}^{d\times d}\,:\,t\in\mathbb{R}^+,\boldsymbol{x}_0\in S_0\subset\mathbb{R}^d\Big\},$$

for some $(d-1)$-dimensional smooth source manifold $S_0\subset\mathbb{R}^d$ and (non-characteristic) initial data $\boldsymbol{p}(0,\boldsymbol{x}_0)=\nabla\phi(\boldsymbol{x}_0)$ on S_0. This is a smooth Lagrangian submanifold of phase space, $\Lambda\subset\mathbb{R}^{d\times d}$, of co-dimension d. Its canonical projection onto physical space, $\Pi:\Lambda\to\mathbb{R}^d$ defined by $\Pi(\boldsymbol{x},\boldsymbol{p})=\boldsymbol{x}$, is invertible as long as the solution is single-valued, *i.e.* there is only one ray from the source that reach $\boldsymbol{x}$. In general, however, Λ will turn back in the $\boldsymbol{x}$-direction and create a multi-valued solution where several points on Λ project on the same $\boldsymbol{x}$. The jacobian of Π is singular where Λ turns back, and the caustic is the projection of these singular points. In differential geometry one shows that, locally, Λ is constrained to a few simple shapes at the caustic. (At least if in addition some stability

under perturbations is demanded.) The caustic can be classified by these shapes and there is thus only a finite number of caustic types (two in 2D and five in 3D), [4, 93]. The most simple one is the *fold* caustic in 2D, for which the local shape of Λ is $[(x=3p_x^2,y),(p_x,p_y)]$.

Since we have the constraint $H(\boldsymbol{x},\boldsymbol{p})=1$, or $|\boldsymbol{p}|=\eta(\boldsymbol{x})$, the dimension of the phase space $(\boldsymbol{x},\boldsymbol{p})$ can actually be reduced by one. We have not done this reduction in the equations above, and (2.14, 2.15), (2.22) and (2.21) are in this sense all overdetermined. We will here show the reduced equations in two dimensions.

Setting $\boldsymbol{p}=\eta(\cos\theta,\sin\theta)$, we can use θ as a dependent variable in (2.14, 2.15) instead of $\boldsymbol{p}$. We then get, with $\boldsymbol{x}=(x,y)$,

$$\frac{dx}{dt}=c(x,y)\cos\theta, \tag{2.23}$$

$$\frac{dy}{dt}=c(x,y)\sin\theta, \tag{2.24}$$

$$\frac{d\theta}{dt}=\frac{\partial c}{\partial x}\sin\theta-\frac{\partial c}{\partial y}\cos\theta. \tag{2.25}$$

Suppose the source is a curve $\boldsymbol{x}_0(r)$ in $\mathbb{R}^2$ parametrized by r, and $\phi(\boldsymbol{x}_0(r))\equiv 0$. Set $\tilde{\boldsymbol{x}}(t,r):=\boldsymbol{x}(t,\boldsymbol{x}_0(r))$ and $\tilde{\boldsymbol{p}}(t,r):=\boldsymbol{p}(r,\boldsymbol{x}_0(r))$. Then $\phi(\tilde{\boldsymbol{x}}(t,r))=t$ by (2.19) and $\boldsymbol{x}_t=\tilde{\boldsymbol{x}}_t\perp\tilde{\boldsymbol{x}}_r$ for all time, since

$$0=\frac{\partial}{\partial r}\phi(\tilde{\boldsymbol{x}}(t,r))=\nabla\phi(\tilde{\boldsymbol{x}})\cdot\tilde{\boldsymbol{x}}_r=\boldsymbol{p}\cdot\tilde{\boldsymbol{x}}_r=\eta^2\tilde{\boldsymbol{x}}_t\cdot\tilde{\boldsymbol{x}}_r.$$

We can then introduce the orthogonal matrix $R:=[\tilde{\boldsymbol{x}}_r\ \tilde{\boldsymbol{x}}_t]$, with determinant $|\det R|=|\tilde{\boldsymbol{x}}_r||\tilde{\boldsymbol{x}}_t|=|\tilde{\boldsymbol{x}}_r|/\eta(\tilde{\boldsymbol{x}})$. By definition, for $0\le s\le t$, we have $\boldsymbol{x}(t,\boldsymbol{x}_0)=\boldsymbol{x}(s,\boldsymbol{x}(t-s,\boldsymbol{x}_0))$, and, by differentiating both sides with respect to t,

$$\boldsymbol{x}_t(t,\boldsymbol{x}_0)=D_{x_0}\boldsymbol{x}(s,\boldsymbol{x}(t-s,\boldsymbol{x}_0))\boldsymbol{x}_t(t-s,\boldsymbol{x}_0).$$

Evaluating at $s=t$ gives

$$\boldsymbol{x}_t(t,\boldsymbol{x}_0)=D_{x_0}\boldsymbol{x}(t,\boldsymbol{x}_0)\boldsymbol{x}_t(0,\boldsymbol{x}_0). \tag{2.26}$$

Therefore $D_{x_0}\boldsymbol{x}(t,\boldsymbol{x}_0(r))R(0,r)=R(t,r)$ and

$$|q(t,\boldsymbol{x}_0(r))|=|\det D_{x_0}\boldsymbol{x}(t,\boldsymbol{x}_0(r))|=\frac{|\det R(t,r)|}{|\det R(0,r)|}=\frac{|\tilde{\boldsymbol{x}}_r(t,r)|\eta(\boldsymbol{x}_0(r))}{|\partial_r\boldsymbol{x}_0(r)|\eta(\tilde{\boldsymbol{x}}(t,r))},$$

so that

$$A(\boldsymbol{x}(t,r))=A(\boldsymbol{x}_0(r))\sqrt{\frac{|\partial_r\boldsymbol{x}_0(r)|\eta(\boldsymbol{x}_0(r))}{|\tilde{\boldsymbol{x}}_r(t,r)|\eta(\tilde{\boldsymbol{x}}(t,r))}}e^{-im\frac{\pi}{2}}. \tag{2.27}$$

We then only need to compute $\tilde{\boldsymbol{x}}_r$ to get the amplitude, which reduces (2.21) to

$$\frac{d}{dt}\begin{pmatrix}\tilde{\boldsymbol{x}}_r\\ \tilde{\boldsymbol{p}}_r\end{pmatrix}=\begin{pmatrix}D^2_{px}H & D^2_{pp}H\\ -D^2_{xx}H & -(D^2_{px}H)^T\end{pmatrix}\begin{pmatrix}\tilde{\boldsymbol{x}}_r\\ \tilde{\boldsymbol{p}}_r\end{pmatrix}. \tag{2.28}$$

2.3 Kinetic equations

Finally, we can adopt a purely kinetic viewpoint. This is based on the interpretation that rays are trajectories of particles following the Hamiltonian dynamics of (2.12, 2.13). We introduce the phase space $(t,\boldsymbol{x},\boldsymbol{p})$, where $\boldsymbol{p}$ is the slowness vector defined above in Section 2.2, and we let $f(t,\boldsymbol{x},\boldsymbol{p})$ be a particle ("photon") density function. It will satisfy the Liouville equation,

$$f_t+\nabla_p H\cdot\nabla_x f-\nabla_x H\cdot\nabla_p f=0, \tag{2.29}$$

or, with $H(\boldsymbol{x},\boldsymbol{p})=c(\boldsymbol{x})|\boldsymbol{p}|$,

$$f_t+\frac{c(\boldsymbol{x})}{|\boldsymbol{p}|}\boldsymbol{p}\cdot\nabla_x f+\frac{|\boldsymbol{p}|}{\eta^2}\nabla_x\eta\cdot\nabla_p f=0. \tag{2.30}$$

We are only interested in solutions to (2.12, 2.13) for which $H\equiv 1$, meaning that f only has support on the sphere $|\boldsymbol{p}|=\eta(\boldsymbol{x})$ in phase space. Because of this we can simplify (2.30) to the Vlasov-type equation

$$f_t+\frac{1}{\eta^2}\boldsymbol{p}\cdot\nabla_x f+\frac{1}{\eta}\nabla_x\eta\cdot\nabla_p f=0, \tag{2.31}$$

with initial data $f_0(\boldsymbol{x},\boldsymbol{p})$ vanishing whenever $|\boldsymbol{p}|\neq\eta$. We note that, if $\eta\equiv 1$, the equation (2.31) is just a free transport equation with solution $f(t,\boldsymbol{x},\boldsymbol{p})=f_0(\boldsymbol{x}-t\boldsymbol{p},\boldsymbol{p})$ which corresponds to straight line ray solutions of (2.14, 2.15).

The Wigner transform provides a direct link between the density function f in (2.31) and the solution to the scalar wave equation (2.1) and the Helmholtz equation (2.9). It is an important tool in the study of high frequency, homogenization and random medium limits of these and many other equations, such as the Schrödinger equation, [11,34,63,82]. The Wigner transform of a solution $u^\omega(\boldsymbol{x})$ at frequency ω is defined by

$$f^\omega(t,\boldsymbol{x},\boldsymbol{p}):=\int_{\mathbb{R}^d}\exp(-i\boldsymbol{y}\cdot\boldsymbol{p})\,u^\omega(t,\boldsymbol{x}+\boldsymbol{y}/2\omega)\overline{u^\omega(t,\boldsymbol{x}-\boldsymbol{y}/2\omega)}d\boldsymbol{y}.$$

If $\{u^\omega\}$ is bounded in $L^2(\mathbb{R}^d)$ (for instance), then a subsequence of $\{f^\omega\}$ converges weakly in $\mathcal{S}'(\mathbb{R}^d)$, the space of tempered distributions, as $\omega\to\infty$, [63]. The limit is a locally bounded nonnegative measure called the Wigner measure or semiclassical measure, which in our case agrees with the density function f in (2.31) above. An important property of the Wigner transform is that, when u^ω is a simple wave,

$$u^\omega(t,\boldsymbol{x})=A(t,\boldsymbol{x})e^{i\omega\phi(t,\boldsymbol{x})}, \tag{2.32}$$

then $f^\omega\to f$ weakly in $\mathcal{S}'$, and the Wigner measure f represents a 'particle' in phase space of the form

$$f(t,\boldsymbol{x},\boldsymbol{p})=A^2(t,\boldsymbol{x})\delta(\boldsymbol{p}-\nabla\phi(t,\boldsymbol{x})). \tag{2.33}$$

We note here that only the gradient of the phase is present and the value of the phase itself disappears in this formulation. Even though f^ω is not linear in u^ω, a sum of simple wave solutions like in (2.4) converges to a sum of "particle" solutions to (2.31),

$$f(t,\boldsymbol{x},\boldsymbol{p}) = \sum_{n=1}^{N} A_n^2(t,\boldsymbol{x})\delta(\boldsymbol{p}-\nabla\phi_n(t,\boldsymbol{x})). \tag{2.34}$$

See [44, 87]. Other references dealing with the rigorous study of the convergence $f^\omega \to f$ and proving that the limiting Wigner measure f satisfies a transport equation such as (2.31) are [6, 18, 70]. We can also derive (2.31) directly from the wave equation (2.1) using so-called H-measures, [91], or microlocal defect measures, [33].

From (2.34) it follows that the total amplitude at a point $\boldsymbol{x}$ is given as the integral of f over the phase variable,

$$A_{\text{tot}}^2(t,\boldsymbol{x}) = \sum_{n=1}^{N} A_n^2 = \int_{\mathbb{R}^d} f(t,\boldsymbol{x},\boldsymbol{p})dp.$$

This is the weak limit of $|u^\omega(t,\boldsymbol{x})|^2$. Because of interference between the waves, A_{tot}^2 is in general not pointwise close to $|u^\omega(t,\boldsymbol{x})|^2$ when there are several crossing waves, $N>1$.

2.4 Boundary and interface conditions

Boundary conditions for the geometrical optics approximation are derived from the boundary conditions for the wave equation. They follow from assuming that a wave incident to the boundary generates a reflected wave, and that they both have smooth phase functions. For Dirichlet and Neumann conditions the reflection law holds

$$\theta_{\text{ref}} = \theta_{\text{inc}}, \tag{2.35}$$

with the notation as in Fig. 2. The amplitudes of the incident and reflected rays are related simply by

$$A_{\text{ref}} = \pm A_{\text{inc}},$$

with negative sign for Dirichlet condition and positive for Neumann condition. There are also boundary conditions for the quantities in (2.21) related to the geometrical spreading, often represented by the wave front's principal radii of curvature. Those conditions depend on the local shape of the boundary.

When a wave hits a sharp interface between two materials there will in general be both a reflected and a transmitted wave, assuming that the width of the interface is much smaller than the wavelength. In this case interface conditions must be derived directly from the wave equation, before passing to the high frequency limit. For simplicity we assume that we have the planar interface in Fig. 2. As before, the phase functions of all

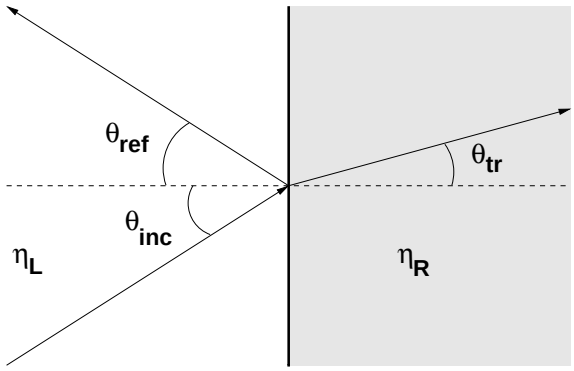

Figure 2: Reflection and transmission of a ray at a sharp interface when $\eta_L < \eta_R$.

involved waves are assumed to be smooth. Continuity of the solution across the interface then gives the reflection law (2.35) for θ_{ref} and *Snell's law* of refraction for θ_{tr},

$$\eta_L \sin\theta_{\text{inc}} = \eta_R \sin\theta_{\text{tr}}. \tag{2.36}$$

(Note, when $\eta_L > \eta_R$ there may be no θ_{tr} satisfying this; if θ_{inc} is greater than a critical angle there is total internal reflection and no transmitted ray.) Interface conditions for the amplitudes and geometrical spreading coefficients depend on the type of wave equation, physics for the problem in question and the local shape of the interface. In the case of the scalar wave equation (2.1), with a plane incident wave and a planar interface, continuity of the solution's normal derivative at the interface implies

$$A_{\text{ref}} = \frac{\eta_L \cos\theta_{\text{inc}} - \eta_R \cos\theta_{\text{tr}}}{\eta_L \cos\theta_{\text{inc}} + \eta_R \cos\theta_{\text{tr}}} A_{\text{inc}}, \qquad A_{\text{tr}} = \frac{2\eta_L \cos\theta_{\text{inc}}}{\eta_L \cos\theta_{\text{inc}} + \eta_R \cos\theta_{\text{tr}}} A_{\text{inc}}.$$

For systems of wave equations, like Maxwell's equations and the elastic wave equation, the situation is a little more complicated. The interface and boundary conditions typically couple the amplitudes of different components, and one incident wave may generate several transmitted and reflected waves. Note that when the interface width is large compared to the wave length, there is only a transmitted wave, and Snell's law follows from the geometrical optics equations.

2.5 Corrections to geometrical optics

The main shortcomings of standard geometrical optics are the failure to include diffraction effects and its breakdown at caustics. In this section we give a brief introduction to how diffracted waves can be added to geometrical optics and how to correct the approximation close to caustics.

2.5.1 Diffraction at nonsmooth boundaries

The geometrical theory of diffraction (GTD) can be seen as a generalization of geometrical optics. It was pioneered by Keller in the 1960s, [52], and provides a technique for

adding diffraction effects to the geometrical optics approximation. GTD is often used in scattering problems in computational electromagnetics, where boundary effects are of major importance, for example in radar cross section calculations and in the optimization of base station locations for cell phones in a city.

In general, diffracted rays are induced at discontinuities in the standard geometrical optics solution. By the reflection law (2.35), this happens primarily at singular points of the boundary, such as at corners and edges where the normal, and therefore the reflected field, is discontinuous. At these points an infinite set of diffracted rays are produced. The diffracted rays obey the usual geometrical optics equations. (The main computational task, even for GTD, is thus based on the standard geometrical optics approximation.) The amplitude of each diffracted ray is proportional to the amplitude of the ray hitting the corner and a diffraction coefficient D. The coefficient D depends on the directions of the inducing and diffracted rays, the frequency, the local boundary geometry and the shape of the incident wave front.

An example is given in Fig. 3 where the incident plane wave is reflected off a half plane. This divides the space into regions A, B and C according to the number ray families present (two, one and zero respectively). The resulting geometrical optics solution is discontinuous at the region interfaces. Infinitely many diffracted rays shoot out in all directions at the singular tip of the half plane, which thus acts as an (anisotropic) point source.

By (2.5) the error in standard geometrical optics solutions is of the order $\mathcal{O}(1/\omega)$. However, the derivation of (2.6) and (2.7) from (2.5) does not take into account the effects of geometry and boundary conditions. In these cases the series expansions (2.5, 2.10) are not adequate and extra terms must be added to match the solution to the boundary conditions. These terms represent the diffracted waves. They are of the order $\mathcal{O}(1/\omega^\alpha)$ for some $\alpha\in(0,1)$ and hence much larger than the usual error in standard geometrical optics, but still small for large frequencies. Discarding diffraction phenomena, may therefore be too crude an approximation for a scattering problem at moderate frequencies.

One typical improved expansion that includes diffraction terms is

$$u(\boldsymbol{x}) = e^{i\omega\phi(\boldsymbol{x})}\sum_{k=0}^{\infty} A_k(\boldsymbol{x})(i\omega)^{-k} + \frac{1}{\sqrt{\omega}}\, e^{i\omega\phi_{\mathrm{d}}(\boldsymbol{x})}\sum_{k=0}^{\infty} B_k(\boldsymbol{x})(i\omega)^{-k}, \tag{2.37}$$

which is similar to the standard geometrical optics ansatz (2.5), only that a new diffracted wave scaled by $\sqrt{\omega}$ has been added (index d). For high frequencies, the diffraction term B_0 is also retained, together with the geometrical optics term A_0. More elaborate expansions must sometimes be used, such as those given by the *uniform theory of diffraction* (UTD), [55].

It is important to note that the diffraction coefficients only depend on the *local* geometry of the boundary. Relatively few types of coefficients are therefore sufficient for a systematic use of GTD. Diffraction coefficients have been computed for many different canonical geometries, such as wedges, slits and apertures, different wave equations, in particular Maxwell equations, and different materials and boundary conditions. For

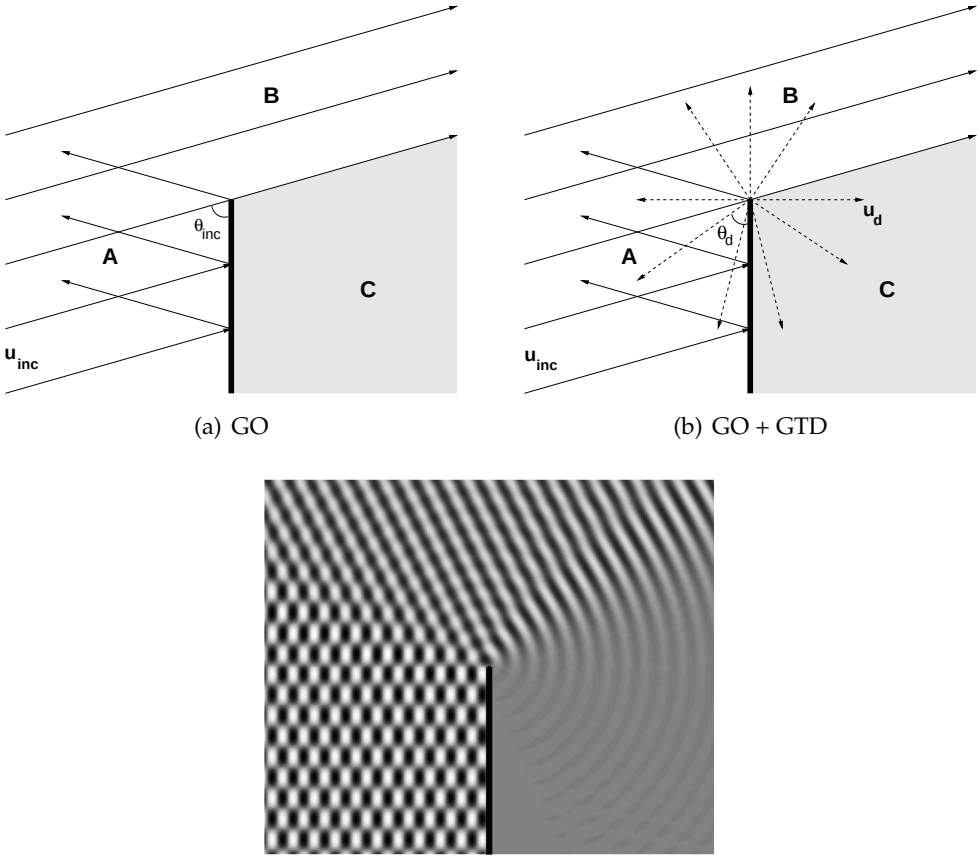

(a) GO (b) GO + GTD

(c) Helmholtz

Figure 3: A typical geometrical optics solution in two dimensions and a constant medium ($c\equiv 1$) around a perfectly reflecting halfplane (a), and the same problem augmented with diffracted waves given by GTD (b). In the geometrical optics case, region A contains two phases (incident and reflected), region B one phase (incident), and region C is in shadow, with no phases and hence a zero solution. On the boundaries between the regions the geometrical optics solution is discontinuous. Real part of a solution to the Helmholtz equation for this problem is shown in (c). The diffracted wave is faintly visible as a circular wave centered at the halfplane tip.

example, in a two-dimensional homogeneous medium the diffraction coefficient D for a halfplane is

$$D(\theta_{\rm d},\theta_{\rm inc},\omega)=\frac{e^{i\pi/4}}{2\sqrt{2\pi\omega}}\left(\frac{1}{\cos\frac{\theta_{\rm d}-\theta_{\rm inc}}{2}}\pm\frac{1}{\cos\frac{\theta_{\rm d}+\theta_{\rm inc}}{2}}\right), \tag{2.38}$$

with the definition of the angles as in Fig. 3a and Fig. 3b. Letting $\boldsymbol{x}_0$ be the position of tip of the halfplane the expression for the diffracted wave, away from $\boldsymbol{x}_0$, is then

$$u_{\rm d}(\boldsymbol{x})=\frac{u_{\rm inc}(\boldsymbol{x}_0)}{\sqrt{|\boldsymbol{x}-\boldsymbol{x}_0|}}D(\theta_{\rm d},\theta_{\rm inc},\omega)e^{-i\omega|\boldsymbol{x}-\boldsymbol{x}_0|}. \tag{2.39}$$

2.5.2 Creeping rays

Another type of diffraction is generated even for smooth scatterers. When an incident field hits a smooth body there will be a shadow zone behind it and the geometrical optics solution will again be discontinuous. There is a curve (point in 2D) dividing the shadow part and the illuminated part of the body. Along this *shadow line* (shadow point in 2D) the incident rays are tangent to the body surface. The shadow line will act as a source for surface rays[†], or *creeping rays*, that propagate along geodesics on the scatterer surface, if the surrounding medium is homogeneous, $\eta \equiv 1$. The creeping ray carries an amplitude proportional to the amplitude of the inducing ray. The amplitude decays exponentially along the creeping ray's trajectory. In three dimensions, the amplitude also changes through geometrical spreading on the surface. At each point on a convex surface the creeping ray emits surface-diffracted rays in the tangential direction, with its current amplitude. Those rays then follow the usual geometrical optics laws. To compute the creeping ray contribution to the field, one thus needs to find geodesics on the scatterer surface in addition to the standard geometrical optics rays. Some examples of how this can be done are given in [20,71,108].

Let $\boldsymbol{x}_0$ be the incident point on the shadow line where the creeping ray starts, $\boldsymbol{x}_1$ the point on the body where the diffracted ray is emitted and $s = |\boldsymbol{x}-\boldsymbol{x}_1|$ the distance from $\boldsymbol{x}_1$ to the field point. A simple approximation of the diffracted field is given by the formula, [61]

$$u_{\rm d}(\boldsymbol{x}) \sim u_{\rm inc}(\boldsymbol{x}_0) D(\boldsymbol{x}_0,\omega) D(\boldsymbol{x}_1,\omega) \sqrt{\frac{\tilde{q}(\boldsymbol{x}_0)}{\tilde{q}(\boldsymbol{x}_1)} \frac{\rho(\boldsymbol{x}_1)}{s(\rho(\boldsymbol{x}_1)+s)}}\, e^{i\omega(t+s)} e^{-\int_0^t \alpha(t',\omega)dt'}.$$

Here D is a diffraction coefficient that depends on the local geometry, $\tilde{q}$ is the surface geometrical spreading and ρ is the local radius of curvature of the creeping wave front. The last integral is taken along the creeping ray, whose length is t. The attenuation α depends on the local curvature of the body.

A 2D example is shown in Fig. 4. When Dirichlet conditions are applied to the cylinder of radius R, we have

$$D(\boldsymbol{x},\omega)^2 = \frac{e^{-i\pi/12}\sqrt{R}}{2^{5/6}\sqrt{\pi}\,\mathrm{Ai}'(-\nu_0)^2} \cdot \frac{1}{(\omega R)^{1/6}}, \qquad \alpha(t,\omega) = \frac{e^{i\pi/6}\nu_0}{2^{1/3}R} \cdot (\omega R)^{1/3},$$

where Ai is the Airy function and ν_0 is the smallest positive zero of $\mathrm{Ai}(-\nu)$. For 2D problems ρ is infinite and $\tilde{q}(\boldsymbol{x}_1)/\tilde{q}(\boldsymbol{x}_0) = 1$. Since α and D are constant in t and $\boldsymbol{x}$ for this case, we simply have

$$u_{\rm d}(\boldsymbol{x}) \sim u_{\rm inc}(\boldsymbol{x}_0) \frac{D(\omega)^2}{\sqrt{s}} e^{i\omega(t+s)} e^{-t\alpha(\omega)},$$

with D and α as above.

[†]Other well-known surface waves are the Rayleigh waves in the elastic wave equation.

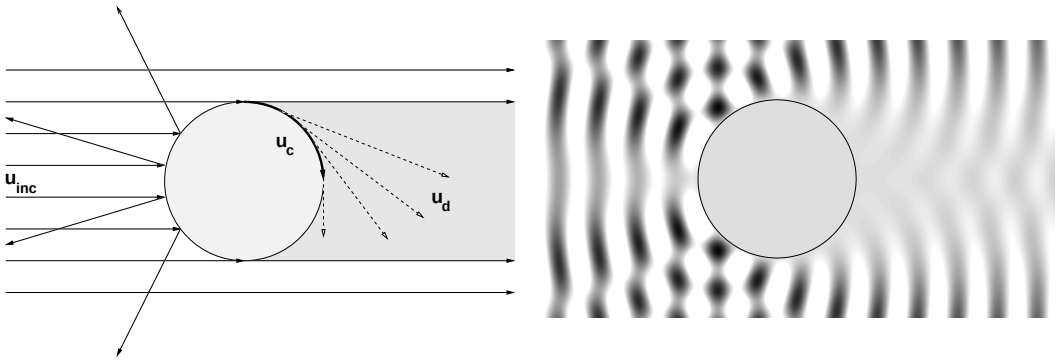

Figure 4: Diffraction by a smooth cylinder. Left figure shows the solution schematically. The incident field u_{inc} induces a creeping ray u_{c} at the north (and south) pole of the cylinder. As the creeping ray propagates along the surface, it continuously emits surface-diffracted rays u_{d} with exponentially decreasing initial amplitude. Right figure shows the real of a solution to the Helmholtz equation. The surface diffracted waves can be seen behind the cylinder.

2.5.3 Caustics

Close to caustics the amplitude grows rapidly in the geometrical optics approximation and blows up at the caustic itself, as discussed in Section 2.2. In reality the amplitude remains bounded, but increases with the frequency ω, see Fig. 5. The error in the standard series expansion (2.5) is thus unbounded around caustics. To capture the actual solution behavior there are better expansions that have small errors uniformly in ω, derived *e.g.* by Ludwig [66] and Kravtsov [56]. The expansions are different for different types of caustics. For a fold caustic there are two ray families meeting at the caustic, with phases ϕ^+ and ϕ^-. Letting $\rho=\frac{3}{4}(\phi^+-\phi^-)$ a more suitable description of the solution u in this case is

$$u(\boldsymbol{x})=\omega^{1/6}e^{i\omega\phi(\boldsymbol{x})}\left(\mathrm{Ai}(-(\omega\rho(\boldsymbol{x}))^{2/3})\sum_{k=0}^{\infty}A_k(\boldsymbol{x})(i\omega)^{-k}\right.$$
$$\left.+i\omega^{-1/3}\mathrm{Ai}'(-(\omega\rho(\boldsymbol{x}))^{2/3})\sum_{k=0}^{\infty}B_k(\boldsymbol{x})(i\omega)^{-k}\right).$$

The dominant term close to the caustic, $|\rho|\omega\ll 1$ is of the order $\mathcal{O}(\omega^{1/6})$ with an error of $\mathcal{O}(\omega^{-1/3})$. Away from the caustic, on the convex side where $\rho>0$, we can use the fact that $|\mathrm{Ai}(-x)|\sim x^{-1/4}$ and $|\mathrm{Ai}'(-x)|\sim x^{1/4}$ for large x, to conclude that the dominant term is of the order $\mathcal{O}(1)$ with an error of $\mathcal{O}(\omega^{-1})$, *i.e.* the standard situation for geometrical optics.

One of the problems at caustics is that multiple ray families meet. To analyze the asymptotic behavior of the wave field close to a caustic one can therefore look at solutions given by an oscillatory integral,

$$u(\boldsymbol{x})=\left(\frac{\omega}{2\pi}\right)^{d/2}\int_{\mathbb{R}^d}A(\boldsymbol{x},\theta)\mathrm{e}^{i\omega\phi(\boldsymbol{x},\theta)}d\theta,$$

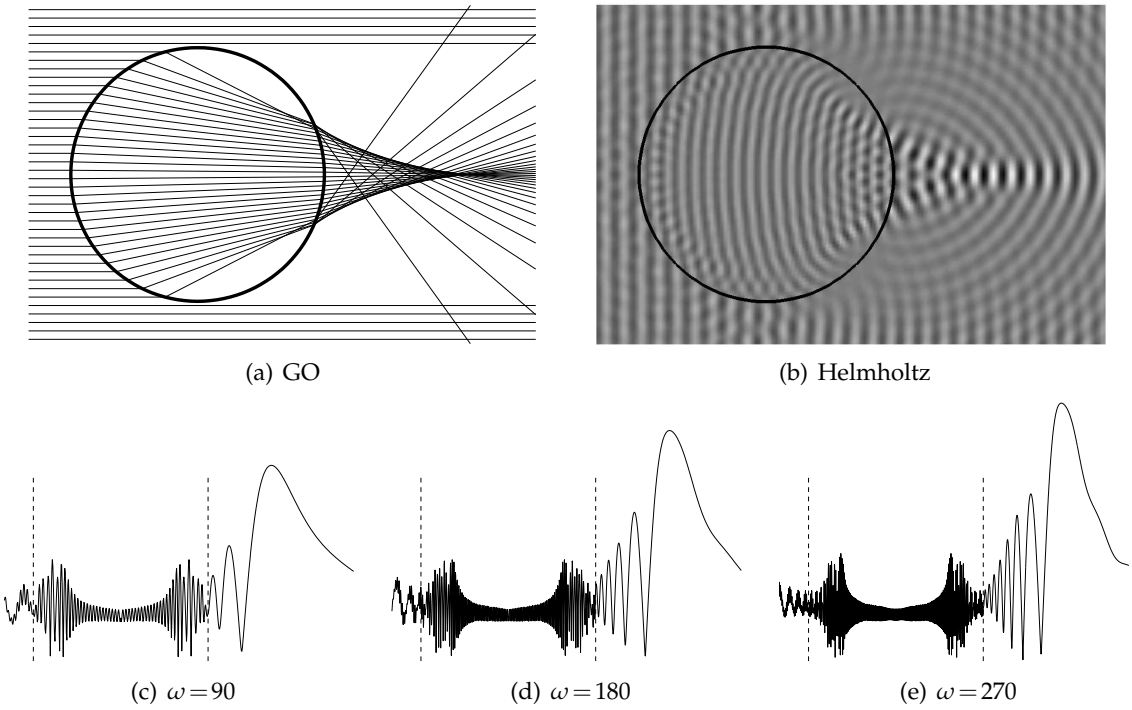

(a) GO (b) Helmholtz

(c) $\omega = 90$ (d) $\omega = 180$ (e) $\omega = 270$

Figure 5: Caustics generated when a plane wave is refracted by a cylinder of higher refractive index than the surrounding media. The geometrical optics solution by ray tracing is shown in (a), while (b) contains an actual solution of Helmholtz equation (real part). The concentration of rays coincides with the pronounced dark/light pattern (high amplitude) in the solution. The figures in the bottom row (c–e) show the absolute value of the Helmholtz solution in a horizontal cut in the middle of the top figures, for increasing frequencies ω. The cylinder boundaries are indicated by dashed lines. The amplitude away from the caustic is independent of ω but grows slowly with ω at the caustic.

which can be seen as a continuous superposition of waves with different phases parameterized by θ (*cf.* also (2.4)). See *e.g.* the works of Maslov [67], Duistermaat [25] and Hörmander [42]. One can show that there is a globally valid representation of this type for the solution, and that the functions $A(\boldsymbol{x},\theta)$ and $\phi(\boldsymbol{x},\theta)$ to leading order satisfy the eikonal and transport equations (2.6, 2.7) for fixed θ. The stationary phase method can be used to find the main contributions of the integral. Nondegenerate stationary points, where $\nabla_\theta \phi = 0$ and the Hessian $D^2_{\theta\theta}\phi$ has full rank, correspond to the usual rays, which are $\mathcal{O}(1)$ solutions. Caustics correspond to degenerate stationary points, with $\nabla_\theta \phi = 0$ and a rank deficient Hessian. These give solutions of size $\mathcal{O}(\omega^\alpha)$, where α depends on the dimension of the null-space of $D^2_{\theta\theta}\phi$.

2.6 Other high frequency models

In this section we will discuss two alternatives to the geometrical optics model: physical optics and gaussian wave packets.

2.6.1 Physical optics

The physical optics (PO) method, also known as Kirchhoff's approximation, combines the geometrical optics solution with a boundary integral formulation of the solution to the Helmholtz equation. It is often used for scattering problems in, e.g., computational electromagnetics. Let Ω be a perfectly reflecting scatterer in $\mathbb{R}^3$, *i.e.* $u=0$ on the boundary $\partial\Omega$, and divide the solution into a (known) incident and an (unknown) scattered part, $u=u_{\text{inc}}+u_{\text{s}}$. Then, in a homogeneous medium with $c\equiv 1$,

$$\Delta u_{\text{s}}+\omega^2 u_{\text{s}}=0, \quad \boldsymbol{x}\in\mathbb{R}^3\setminus\overline{\Omega}, \tag{2.40}$$

$$u_{\text{s}}=-u_{\text{inc}}, \qquad \boldsymbol{x}\in\partial\Omega, \tag{2.41}$$

together with an outgoing radiation condition. The solution outside Ω is given by the integral

$$u_{\text{s}}(\boldsymbol{x})=-\oint_{\partial\Omega} u_{\text{inc}}(\boldsymbol{x}')\frac{\partial G(\boldsymbol{x},\boldsymbol{x}')}{\partial n}+G(\boldsymbol{x},\boldsymbol{x}')\frac{\partial u_{\text{s}}(\boldsymbol{x}')}{\partial n}d\boldsymbol{x}', \tag{2.42}$$

where G is the free space Green's function in three dimensions:

$$G(\boldsymbol{x},\boldsymbol{x}')=\frac{e^{i\omega|\boldsymbol{x}-\boldsymbol{x}'|}}{4\pi|\boldsymbol{x}-\boldsymbol{x}'|}.$$

The unknown in this, exact, expression for the solution is $\partial_n u_{\text{s}}$ on the boundary of Ω. In physical optics, this unknown is simply replaced by the geometrical optics solution. For example, let $\hat{\boldsymbol{n}}(\boldsymbol{x})$ be the normal of $\partial\Omega$ at $\boldsymbol{x}$ and assume that the incident field is a plane wave $u_{\text{inc}}(\boldsymbol{x})=\exp(-i\omega\boldsymbol{k}\cdot\boldsymbol{x})$, with $|\boldsymbol{k}|=1$ and that Ω is convex. Then we would use the approximation

$$\frac{\partial u_{\text{s}}(\boldsymbol{x})}{\partial n}\approx -i\omega|\boldsymbol{k}\cdot\hat{\boldsymbol{n}}(\boldsymbol{x})|e^{-i\omega\boldsymbol{k}\cdot\boldsymbol{x}}, \qquad \boldsymbol{x}\in\partial\Omega. \tag{2.43}$$

Note that this approximation would be applied both in the illuminated and shadow part of $\partial\Omega$. In the so-called *physical theory of diffraction* (PTD), the GTD extension of the geometrical optics solution is used instead.

Expression (2.42) gives a rigorous pointwise solution to the Helmholtz in free space, regardless what is used for $\partial_n u_{\text{s}}$. The PO approximation is made at the boundary and it is not self-consistent for finite frequencies: The normal derivative of u_{s} at the boundary, computed from (2.42), is not equivalent to the applied geometrical optics solution in (2.43). Iterative schemes to obtain this consistency can be used.

The accuracy of the PO approximation increases with frequency. Writing

$$\frac{\partial u_{\text{s}}(\boldsymbol{x})}{\partial n}=A(\boldsymbol{x},\omega)e^{-i\omega\boldsymbol{k}\cdot\boldsymbol{x}},$$

one can show that for convex smooth scatterers,

$$A(\boldsymbol{x},\omega)+i\omega|\boldsymbol{k}\cdot\hat{\boldsymbol{n}}(\boldsymbol{x})|=\mathcal{O}(1),$$

away from shadow lines (*cf.* Section 2.5.2). At a shadow line, where $\boldsymbol{k}\cdot\hat{\boldsymbol{n}}(\boldsymbol{x})\approx 0$, the error estimate degenerates to $\mathcal{O}(\omega^{2/3})$. See [69].

The computational cost for PO is lower than the direct solution of the boundary integral formulation of the wave equation. Unlike geometrical optics, however, the cost of finding the solution u_s is typically not frequency-independent, but grows with frequency since (2.42) must be evaluated and there are small scales in $G(\boldsymbol{x},\boldsymbol{x}')$.

The PO approximation has also been used as a stepping stone to solve the full integral equation (2.42) with a low complexity. These methods are based on the observation that $A(\boldsymbol{x},\omega)$ oscillates much slower than $\partial_n u_s$, and can be used as the unknown instead, to reduce the number of degrees of freedom. See *e.g.* [1,2] and more recently [15,24,59].

2.6.2 Gaussian wave packets

Gaussian wave packets, or *gaussian beams*, is another way to describe high frequency waves, [5,79]. It is related to ray tracing, but instead of viewing rays just as characteristics of the eikonal equation, gaussian beams are "fatter" rays: They are full (approximate) solutions to the wave equation or the Helmholtz equation in a narrow support around the path of a standard ray. The main advantage of this description is that it is able to handle caustics correctly; the predicted amplitudes always remain bounded. Gaussian wave packets are also used in quantum mechanics, where they are solutions to the Schrödinger equation representing paths of near-classical particles, [40].

The starting point for analyzing gaussian wave packets is the usual WKB ansatz

$$u(\boldsymbol{x}) = e^{i\omega\phi(\boldsymbol{x})}\sum_{k=0}^{\infty} a_k(\boldsymbol{x})(i\omega)^{-k}.$$

We are interested in solutions of this type in a neighborhood of a ray $\boldsymbol{x}(t)$, satisfying the ODE system (2.12, 2.13) together with $\boldsymbol{p}(t)$. In order to construct a solution mainly supported close to $\boldsymbol{x}(t)$ we let ϕ have a *positive imaginary part* away from $\boldsymbol{x}(t)$. The solution will then be exponentially decreasing away from $\boldsymbol{x}(t)$. In practice only the values of the phase ϕ and the Hessian $D^2\phi$ on the ray are used. Then, letting $\boldsymbol{y}$ be orthogonal to $\boldsymbol{x}_t(t)$ and $\nabla\phi$, we take the small $\boldsymbol{y}$ Taylor expansion,

$$u(\boldsymbol{x}(t)+\boldsymbol{y}) \approx e^{i\omega[\phi(\boldsymbol{x}(t))+\frac{1}{2}\boldsymbol{y}^T D^2\phi(\boldsymbol{x}(t))\boldsymbol{y}]}a_0(\boldsymbol{x}(t)),$$

as an approximation to the exact solution. Although only quantities on the ray $\boldsymbol{x}(t)$ appears in this expression, the phase and amplitude are defined also away from it. Note that ϕ is constructed based on one specific ray (the center ray of the beam), which is not the case in standard geometrical optics where it is globally defined for all rays. As an example we consider the simple two-dimensional case, with the straight ray $\boldsymbol{x}(t) = (x(t),y(t)) = (t,0)$ and let $\phi_{yy}(x,0) = a(x)+ib(x)$ with $b>0$. Noting that $\nabla\phi(\boldsymbol{x}(t)) = (1,0)^T$ we can find the expression for u to leading order in y,

$$u(x,y) \approx e^{i\omega[\phi(x,0)+\frac{y^2}{2}a(x)]}e^{-b(x)\omega y^2/2}a_0(x,0).$$

Hence, the profile of the wave packet is essentially gaussian, and it becomes more narrow for high frequencies.

For the construction to make sense, we need to verify that a number of things hold on the ray. First, $\boldsymbol{x}$, $\boldsymbol{p}$, ϕ should obviously be real and $\nabla\phi$ should be parallel to $\boldsymbol{x}_t$. Second, $D^2\phi$ should exist and its imaginary part should be positive definite in the subspace orthogonal to $\boldsymbol{x}_t$. We will show below that these properties are indeed kept for all time if present at $t=0$.

The first point is rather easy to see. Allowing the phase and amplitude to be complex does not change the previous derivation of the eikonal and transport equations (2.6, 2.7, 2.11). If we suppose that $\boldsymbol{p}(0)=\nabla\phi(\boldsymbol{x}_0)$ is real, then clearly $\boldsymbol{x}$, $\boldsymbol{p}$ are real for all t since they are solutions to (2.12, 2.13). We also obtain the earlier identities $\nabla\phi(\boldsymbol{x}(t))=\boldsymbol{p}(t)$ and $\phi(\boldsymbol{x}(t))=\phi(\boldsymbol{x}_0)+t$ from (2.17, 2.18), showing that $\boldsymbol{x}_t$ is parallel to $\nabla\phi$ and ϕ is real for all t, if $\phi(\boldsymbol{x}_0)$ is real.

For the second point, we note first that in standard geometrical optics, it is not true that $D^2\phi$ exists for all times. In fact, it blows up at caustics. Here, however, $D^2\phi$ always exists, and it can be shown as follows. We parameterize the bicharacteristics by their initial position as before, $\tilde{\boldsymbol{x}}=\tilde{\boldsymbol{x}}(t,\boldsymbol{y})$ and $\tilde{\boldsymbol{p}}=\tilde{\boldsymbol{p}}(t,\boldsymbol{y})$ with $\boldsymbol{x}(t):=\tilde{\boldsymbol{x}}(t,\boldsymbol{x}_0)$ and $\boldsymbol{p}(t):=\tilde{\boldsymbol{p}}(t,\boldsymbol{x}_0)$. The relation $\tilde{\boldsymbol{p}}(0,\boldsymbol{y})=\nabla\phi(\boldsymbol{y})$ is also understood. Moreover, we introduce the shorthand notation $J(t):=D_y\tilde{\boldsymbol{x}}(t,\boldsymbol{x}_0)$, $P(t):=D_y\tilde{\boldsymbol{p}}(t,\boldsymbol{x}_0)$ and $C(t):=\Im D^2\phi(\tilde{\boldsymbol{x}}(t,\boldsymbol{x}_0))$. Then the equations (2.21) for J and P can be derived in the same way as before,

$$\frac{d}{dt}\begin{pmatrix}J\\P\end{pmatrix}=\begin{pmatrix}D^2_{px}H & D^2_{pp}H\\ -D^2_{xx}H & -(D^2_{px}H)^T\end{pmatrix}\begin{pmatrix}J\\P\end{pmatrix},\qquad J(0)=I,\quad P(0)=D^2\phi(\boldsymbol{x}_0). \tag{2.44}$$

We note that J and P may now also be complex, since $P(0)=D^2\phi(\boldsymbol{x}_0)$ is complex. We want to show that, for all $t\geq 0$, the Hessian $D^2\phi(\boldsymbol{x}(t))$ exists and $C(t)$ is positive definite in the subspace orthogonal to $\boldsymbol{x}_t(t)$. Our assumption is that this is true for $t=0$. The explanation below is based on [79].

We start by using (2.21) and noting that for any $\boldsymbol{z}\in\mathbb{C}^d$

$$\begin{aligned}&\frac{d}{dt}\Im\boldsymbol{z}^*J^*(t)P(t)\boldsymbol{z}=\Im\boldsymbol{z}^*\frac{dJ^*}{dt}P\boldsymbol{z}+\Im\boldsymbol{z}^*J^*\frac{dP}{dt}\boldsymbol{z}\\ =&\Im\boldsymbol{z}^*\left(D^2_{px}HJ+D^2_{pp}HP\right)^*P\boldsymbol{z}-\Im\boldsymbol{z}^*J^*\left(D^2_{xx}HJ+(D^2_{px}H)^TP\right)\boldsymbol{z}\\ =&\Im\boldsymbol{z}^*P^*D^2_{pp}HP\boldsymbol{z}-\Im\boldsymbol{z}^*J^*D^2_{xx}HJ\boldsymbol{z}=0,\end{aligned}$$

since H is real and $D^2_{xx}H$, $D^2_{pp}H$ are both symmetric. Moreover, since $\boldsymbol{p}_t=D^2\phi\boldsymbol{x}_t$ is real, we have $C(t)\boldsymbol{x}_t(t)=0$ for all $t\geq 0$. Therefore, using also the fact that $D^2\phi(\boldsymbol{x}_0)$ is symmetric, it follows that

$$\begin{aligned}&\Im\boldsymbol{z}^*J^*(t)P(t)\boldsymbol{z}=\Im\boldsymbol{z}^*J^*(0)P(0)\boldsymbol{z}=\Im\boldsymbol{z}^*D^2\phi(\boldsymbol{x}_0)\boldsymbol{z}=\boldsymbol{z}^*C(0)\boldsymbol{z}\\ =&(\boldsymbol{z}_r^\perp)^TC(0)\boldsymbol{z}_r^\perp+(\boldsymbol{z}_i^\perp)^TC(0)\boldsymbol{z}_i^\perp\geq 0,\end{aligned}$$

where $z=z_r+iz_i$ and $\perp$ denotes the projection on the subspace orthogonal to $x_t(0)$. This means that $J(t)z\neq 0$ whenever z_r or z_i is not parallel to $\tilde{x}_t(0,x_0)$. On the other hand, $J(t)\tilde{x}_t(0,x_0)=\tilde{x}_t(t,x_0)\neq 0$ by (2.26), and we conclude that $J(t)$ is nonsingular for all t. (Compare Section 2.2 where we showed that $\det J=q$ vanishes at caustics.) Moreover,

$$P(t)=D_{x_0}\nabla\phi(\tilde{x}(t,x_0))=D^2\phi(\tilde{x}(t,x_0))J(t)$$

and therefore

$$D^2\phi(\tilde{x}(t,x_0))=P(t)J^{-1}(t) \tag{2.45}$$

is always well-defined and uniformly bounded in any fixed time interval. It remains to show that $y^TC(t)y>0$ for all $y\in\mathbb{R}^d$ such that $y^T\tilde{x}_t(t,x_0)=0$ and all $t>0$. Let y be such a vector and define z as the solution to $J(t)z=y$. Then z cannot be parallel to $x_t(0)$ by (2.26) and consequently,

$$y^TC(t)y=\Im z^*J^*(t)P(t)z=(z_r^\perp)^TC(0)z_r^\perp+(z_i^\perp)^TC(0)z_i^\perp>0.$$

For the amplitude we use a somewhat different formula than in the standard geometrical optics case. As before, the first amplitude term a_0 is governed by the transport equation (2.11). On the curve, we note that $a_0(x(t))$ therefore satisfies the ODE

$$\frac{d}{dt}a_0(x(t))=\frac{dx}{dt}\cdot\nabla a_0=\frac{1}{\eta^2}\nabla\phi\cdot\nabla a_0=-\frac{1}{2\eta^2}\Delta\phi(x(t))a_0(x(t)). \tag{2.46}$$

We can compute $\Delta\phi=\operatorname{tr}D^2\phi$ on the curve, by using (2.44, 2.45), and therefore solve (2.46) as an ODE to obtain also a_0 on the curve. The amplitude is bounded since the Hessian $D^2\phi$ is bounded. Note, however, that a_0 may have an imaginary part.

In conclusion we can construct an approximate solution to the Helmholtz equation by solving ODEs similar to ray tracing for x, ϕ, $\nabla\phi$, $D^2\phi$ and a_0. This solution is only supported in a narrow band around a ray, but by the superposition principle such solutions can be added. The full wave field can therefore be approximated by the sum of many gaussian wave packet solutions. To compute it we use initial data for the wave packets that well approximate the wave data at the source, and then solve ODEs for each of them.

3 Numerical methods

In this section we shall describe different classes of computational techniques, based on the three different mathematical models for geometrical optics discussed in Section 2 above: see Fig. 6. We begin by illustrating the advantages and disadvantages of some of the methods by looking at a particular problem in Figs. 7 and 8. The problem in question is a wave with a sharp front (which contains high frequencies) that propagates in a heterogeneous medium. A snap shot of the full wave equation solution is shown in Fig. 7(b). The faint fronts in the upper part of these figures represent reflections and are not captured by geometrical optics but they vanish in the limit as $\omega\to\infty$.

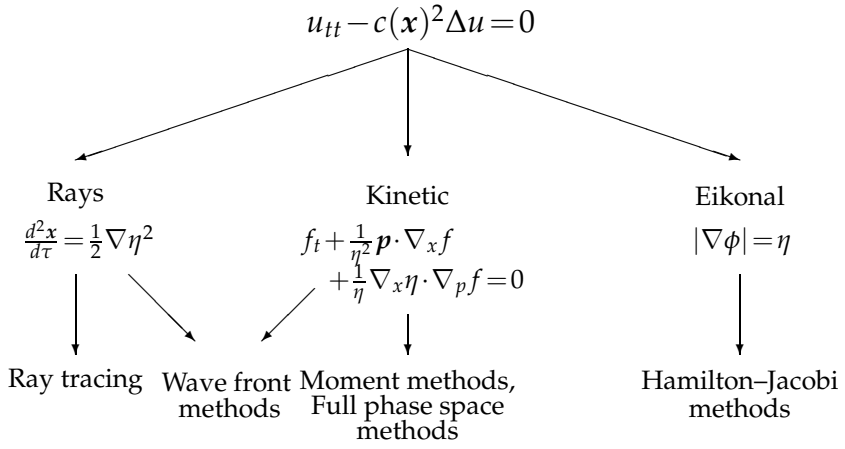

Figure 6: Mathematical models and numerical methods. Wave front methods use aspects of both the ray and the kinetic model.

The traditional way to compute travel times of high-frequency waves is through ray tracing, see Section 3.1. Fig. 8(c) shows one problem with ray tracing: it may produce diverging rays that fail to cover the domain. Even for smooth $c(\boldsymbol{x})$ there may be shadow zones where the field is hard to resolve. This effect derives from the Lagrangian formulation of the problem. The computation follows the flow of the rays, but one would like to obtain the solution on a fixed domain with uniform resolution in space. With ray tracing it is also difficult to compute the amplitude and to find the minimum travel time in regions where rays cross.

More recently, computational methods based on PDEs have been proposed to avoid some of the drawbacks of ray tracing. Interest was initially focused on solving the eikonal equation (1.3) numerically, on a fixed Eulerian grid. Upwind finite difference methods have been used to compute the viscosity solution of (1.3), which is discussed further in Section 3.2. A drawback of (1.3), visible in Fig. 8(a), is that it cannot produce solutions with multiple phases, corresponding to crossing rays. There is no superposition principle. At points where the correct physical solution should have a multivalued phase, the viscosity solution picks out the phase corresponding to the first arriving wave, [23]. Hence, the eikonal equation only gives the first arrival travel time and misses later arrivals, *cf.* Fig. 8(b). A multivalued solution can, however, be constructed by patching together the solutions of several eikonal equations, but this can be difficult; see Section 3.2.

In Section 3.3 *wave front methods* are introduced. They are related to ray tracing, but instead of individual rays, the location of many rays coming from one source is computed, at fixed times. Those points form a wavefront and its evolution is tracked in the physical or the phase space, see Fig. 7(c). The tracking can be done by a pure Lagrangian front tracking method, or Eulerian methods like the segment projection method or level set methods.

The Liouville equation (1.6) has the advantage of the linear superposition property

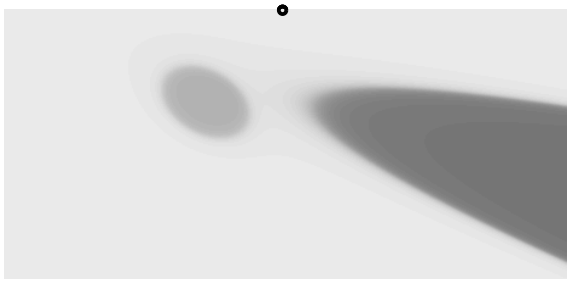

(a) Index of refraction and source point, marked by a circle

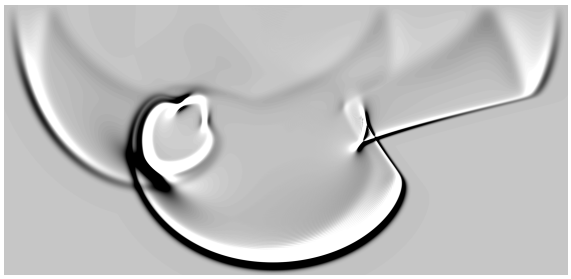

(b) Wave equation solution

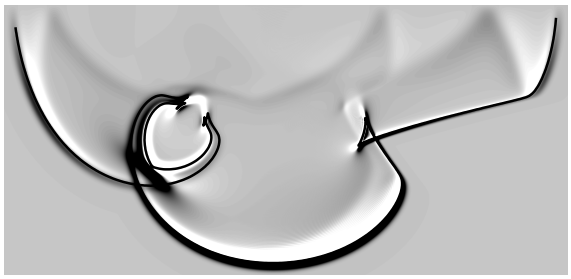

(c) Wave equation solution and wave front

Figure 7: Comparison between different techniques for the same problem. A wave propagates from a point source through a heterogeneous medium. Top figure shows the source and the index of refraction of the medium. Dark and light areas represent high and low index of refraction, respectively. Middle figure shows a snapshot of a resolved numerical solution of the wave equation, where the solution is represented by gray scale levels. Bottom figure shows the same solution with a wave front solution overlaid.

of the ray equations and like the eikonal equation, the solution is defined by a PDE and can easily be computed on a uniform Eulerian grid. Direct numerical approximation of (1.6) is, however, rather costly, because of the large set of independent variables (six in 3D). One way to remedy this problem is based on reducing the number of independent variables by introducing equations for moments, reviewed in Section 3.4. Those *moment methods* rely on the closure assumption that only a finite number of rays cross at each point in time and space. Then f in the Liouville equation (1.6) is of a special form, and it

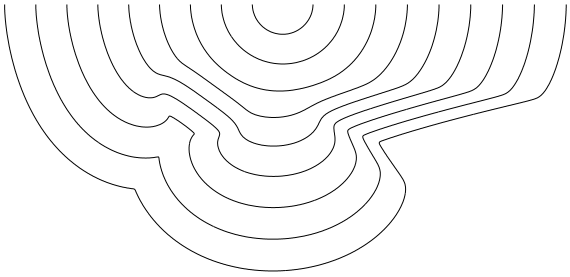

(a) Eikonal equation solution

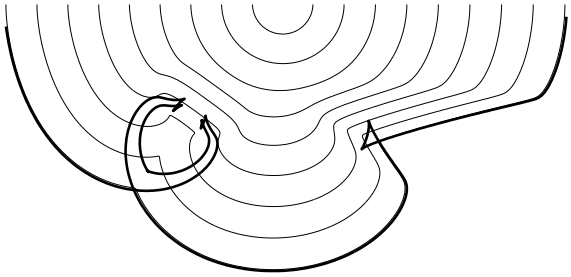

(b) Eikonal equation solution and wave front

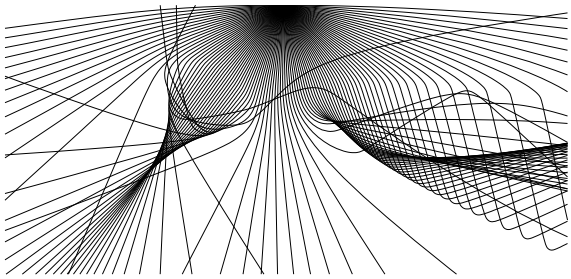

(c) Ray-traced solution

Figure 8: Comparison between different techniques for the same problem. Top figure shows iso curves of a solution to the eikonal equation. Middle figure shows the same solution with a wave front solution overlaid. Bottom figure shows a ray-traced solution.

can be transformed into a finite system of equations representing the moments of f, set in the reduced space $(t,\boldsymbol{x})$.

Another situation when solving the whole Liouville equation can be cost effective, is when the solution is sought for many different sources, but with the same index of refraction. Then *full phase space methods* are an option. See Section 3.5.

Finally, a short examination of *hybrid* methods, which couple both direct and asymptotic solvers, is given in Section 3.6.

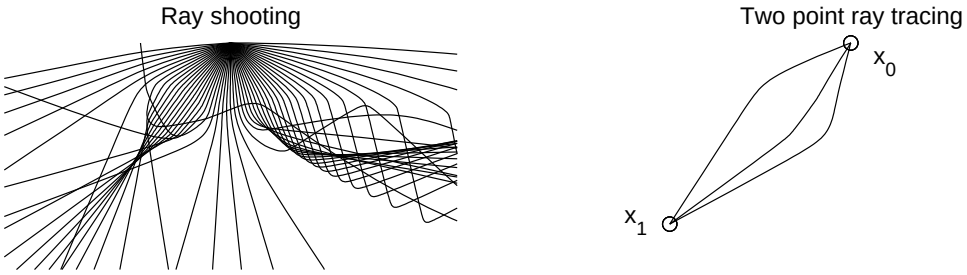

Figure 9: Ray shooting and two point ray tracing. In this case there are three solutions to the two point ray tracing problem.

3.1 Ray tracing

The ray equations derived in Section 2.2 are the basis for ray tracing. The ray $\boldsymbol{x}(t)$ and slowness vector $\boldsymbol{p}(t)=\nabla\phi(\boldsymbol{x}(t))$ are governed by the ODE system (2.14, 2.15). This system can be augmented by another ODE system for the amplitude, (2.21). Solving those ODEs is called ray tracing and it can be regarded as the method of characteristics applied to the eikonal equation. Some general references on ray tracing are [19, 50, 58, 94].

Ray tracing is typically not used to solve the complete Cauchy problem, with arbitrary initial and boundary data. Rather, the interest is to find the travel time of a wave from one source point to all points in a domain, or to a limited set of receiver points, together with the corresponding amplitudes in those points. The initial data is thus a single point source. In applications the same information is often needed for many source points, such as all points on a curve. The procedure is then repeated for each source point.

Ray tracing gives the phase and the amplitude along the rays, and there is no apriori control of which points the ray passes through. One way of obtaining the solution at the particular points of interest is to use *ray shooting:* see Fig. 9 (left). A great many rays are shot from the source point in different directions. The result at the desired receiver points is interpolated from the solutions along the rays. This method is preferred when the travel time is sought for many receiver points, such as the grid points of a discretized domain. The ODEs are solved with standard numerical methods, for instance second or forth order Runge-Kutta methods. The index of refraction is often only given on a grid, and it must be interpolated for the method to work. The interpolation can be smooth, such that the gradient of η in (2.15) exists everywhere, but also simple piecewise constant or linear interpolation is used. The rays are then straight lines or circular arcs within the grid cells, and they can be propagated exactly without an ODE solver. Snell's law of refraction is used at cell boundaries. Interpolating the ray solutions to a uniform grid from a large number of rays is difficult, in particular in shadow zones where few rays penetrate, and in regions where many families of rays cross: *cf.* Fig. 9.

Another strategy to obtain the solution at a particular point is *two point ray tracing*, also known as *ray bending:* see Fig. 9 (right). It is often used when there are only a limited number of receiver points. In this setting the ODEs are regarded as a nonlinear elliptic

boundary value problem. After rescaling $dt=\eta(\boldsymbol{x}(t))^2 d\tau$, we get from (2.14, 2.15),

$$\begin{aligned}&\frac{d^2\boldsymbol{x}}{d\tau^2}=\frac{1}{2}\nabla\eta(\boldsymbol{x}(\tau))^2,\\&\boldsymbol{x}(0)=\boldsymbol{x}_0,\quad \boldsymbol{x}(\tau^*)=\boldsymbol{x}_1,\end{aligned}\tag{3.1}$$

where $\boldsymbol{x}_0$ is the source point and $\boldsymbol{x}_1$ is the receiver point of interest: see *e.g.* [76]. Note that τ^*, the parameter value at the end point $\boldsymbol{x}_1$, is an additional unknown that must be determined together with the solution. The equation (3.1) can be solved by a standard shooting method. It can also be discretized and turned into a nonlinear system of equations that can be solved with, for instance, variants of Newton's method. Initial data for the iterative solver can be difficult to find, in particular if there are multiple solutions (arrivals). Also for two point ray tracing the index of refraction must be interpolated.

In most problems in computational electromagnetics (CEM) the medium is piecewise homogeneous. This simplifies the calculations, since the solution of (2.14, 2.15) is trivial given the solution at the boundaries and on the interfaces between media. Rays are straight lines satisfying the reflection law and Snell's law at interfaces. Ray tracing then reduces to the geometrical problem of finding points where rays are reflected and refracted. In the electromagnetic community, ray shooting is often referred to as *shooting and bouncing rays* (SBR), and two point ray tracing as ray tracing: see *e.g.* [62].

Note that the source and receiver points may be at infinity, corresponding to incident and scattered plane waves. For instance, a common problem in CEM is to compute the radar cross section of an object. In this case both the source and receiver points are typically at infinity.

3.2 Hamilton–Jacobi methods

To avoid the problem of diverging rays, several PDE-based methods have been proposed for the eikonal and transport equations (2.6, 2.7, 2.11). When the solution is sought in a domain, this is also computationally a more efficient and robust approach. The equations are solved directly, using numerical methods for PDEs, on a uniform Eulerian grid to control the resolution.

3.2.1 Viscosity solutions

The eikonal equation is a Hamilton–Jacobi-type equation and it has a unique viscosity solution which represents the first arrival travel time, [23]. This is also the solution to which monotone numerical finite difference schemes converge, and computing it was the starting point for a number of PDE based methods. In [103] and [102] upwind methods were used to compute the viscosity solution of the frequency domain eikonal equation

$$|\nabla\phi|=\eta.\tag{3.2}$$

Upwind methods are stable, monotone methods that give good resolution of the kinks usually appearing in a viscosity solution. Importantly, the methods in [103] and [102] are

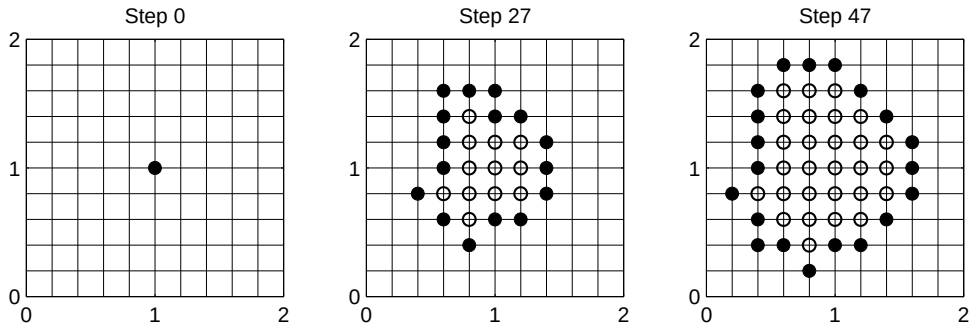

Figure 10: An explicit solver for the frequency domain eikonal equation (3.2). Starting from one source point (left), the grid points are updated one at a time in a certain order (middle, right). The outermost points (filled circles) constitute the grid wave front, which propagates outwards from the source, leaving behind it points where the solution is already established (circles). Note, the grid wave front is not necessarily close to an actual wave front.

explicit; computing the solution at a new grid point only involves previously computed solutions at adjacent grid points. The methods make one sweep over the computational domain, finding the solution at one grid point after another, following an imagined expanding "grid wave front," propagating out from the source: see Fig. 10. To ensure causality and to obtain the correct viscosity solution from an explicit scheme, the grid points must be updated in a certain order. Those early methods used a grid wave front with fixed shape (rectangular in [103] and circular in [102]) and fail in this respect when there are rays in the exact solution that run parallel to the grid wave front. To avoid failure, the grid wave front could systematically be advanced from the grid point that has the smallest current solution value (minimum travel time). This ensures causality and guarantees a correct result, which was recognized in [78]. The method presented in [78] included simple sorting of the points on the grid wave front according to solution value. The sorting was improved in [17], where an efficient heap sort algorithm was proposed to maintain the right ordering of the points on the grid wave front, as it is advanced. The method in [17] bears a close resemblance to the *fast marching method*, [83, 84, 101]. This is an upwind based method for efficient evaluation of distances or generalized distance functions such as the phase ϕ in (3.2). It also uses a heap sort algorithm allowing for computationally efficient choices of marching directions. Those methods can be seen as versions of Dijkstra's algorithm for finding the shortest path in a network, adapted to a grid based setting. The overall computational complexity for solving a problem with N grid points, is $\mathcal{O}(N\log N)$, but it can be reduced to $\mathcal{O}(N)$ with a careful implementation [107]. Other recent $\mathcal{O}(N)$ methods include the *group marching method*, [53] and the *fast sweeping method* [13, 51, 100].

In parallel, high resolution methods of ENO and WENO type, which for some time had been used in the numerical analysis of nonlinear conservation laws, were adapted to Hamilton–Jacobi-equations, [75]. Those methods were used for the time-dependent eikonal equation (2.6) in [30]. Constructing higher order schemes for methods that use

an expanding grid wave front is difficult if the shape of the front changes, as in the fast marching method. For methods with fixed shape grid fronts, the high-resolutions methods can be applied directly to obtain higher order schemes. *Post sweeping* is a technique for avoiding the failures that are associated with turning rays in these methods. The problem at hand is solved in several "sweeps," using different preferred directions. For each sweep, at each grid point, the smallest of the new and the previously computed solution value is selected, [54].

3.2.2 Multivalued solutions

The eikonal and transport equations only describe one unique wave (phase) at a time. There is no superposition principle in the nonlinear eikonal equation. At points where the correct solution should have a multivalued phase, the viscosity solution picks out the phase corresponding to the first arriving wave. When later arriving waves are also of interest, the viscosity solution is not enough. In inverse seismic problems, for instance, it is recognized that first arrival travel times are often not sufficient to give a good migration image, [32]. This is particularly a problem in complicated inhomogeneous media, where caustics that generate new phases appear in the interior of the computational domain for almost any type of source. The problem is related to the fact that the first arrival wave is not always the most energetic one (*cf.* the example in Figs. 7 and 8).

One way to obtain more than the first arrival solution is to geometrically decompose the computational domain, and solve the eikonal solution, with appropriate boundary conditions, in each of the subdomains. The viscosity solutions thus obtained, can be pieced together to reconstruct a larger part of the full multibranch solution.

A simple decomposition strategy can be based on detecting kinks in the viscosity solution. The kinks appear where two different branches of the full solution meet, *cf.* Section 2.1. In [30] an attempt was made to compute multivalued travel times with this approach. A second phase, corresponding to the second arrival time, was calculated using two separate viscosity solutions of the eikonal equation, with boundary conditions for the second phase given at the location of the kink that had appeared in the first viscosity solution, see Fig. 11. The same technique was also used at geometric reflecting boundaries. In principle, the same procedure could be repeated, using kinks in the second solution as boundary data for a third phase, etc.

It is difficult, however, to find a robust way of detecting a kink and to distinguish it from rapid, but smooth, gradient shifts at strong refractions. For more complicated problems, such as the one shown in Fig. 12, there are difficulties even if the kink could be detected perfectly. In this example, there is no obvious way to find boundary data for the third phase using the singularities in the second viscosity solution (bottom row, middle figure). Moreover, only the part of the second solution lying to the right of the caustic curve that develops (see ray-traced solution), corresponds to a physical wave. The rest of the solution should be disregarded, including the kinks near the top and bottom right corners.

Another, more ad hoc, way of dividing the domain is used in the *big ray tracing*

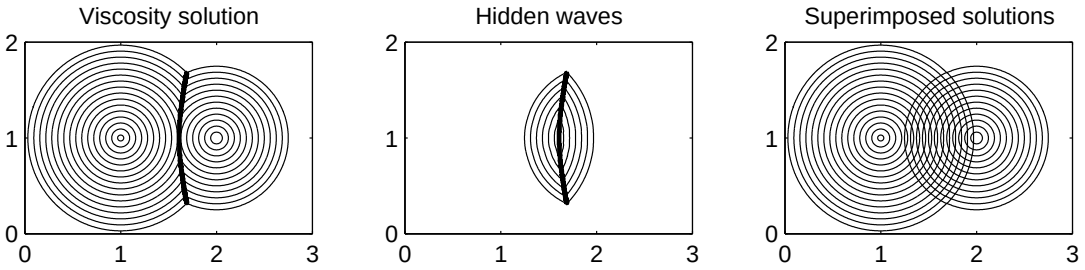

Figure 11: Geometrical decomposition by detecting kinks. Bold lines indicate location of the (first) viscosity solution kink. Middle figure shows second viscosity solution where the first solution (left) was applied as boundary condition at the kink.

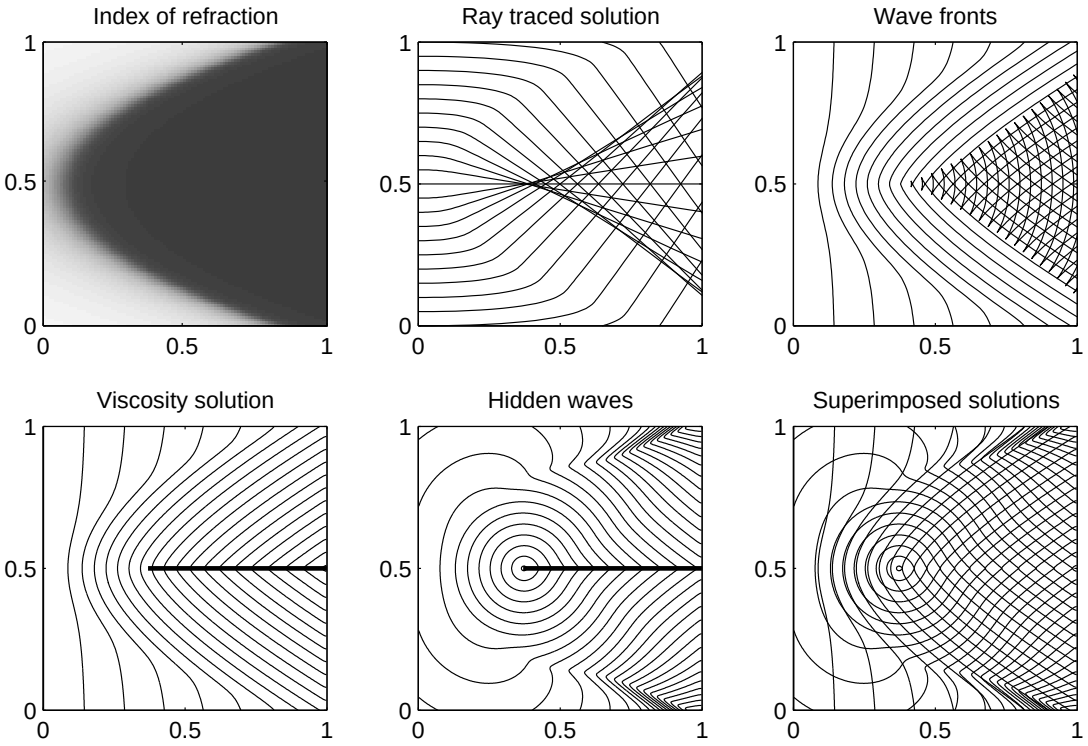

Figure 12: Geometrical decomposition by detecting kinks in a problem with a caustic. Top row shows index of refraction and exact solution. Bottom row shows computed solutions. Bold lines indicate location of the (first) viscosity solution kink.

method. It was introduced in [8], and extended for use with unstructured grids in [3]. A limited number of rays are shot from the source point in different directions. The domains bounded by two successive rays are the "big rays." In each big ray, the viscosity solution is computed. Since the big rays may overlap multivalued solutions can be obtained, although in general the method will not capture all phases. In the presence of caustics the basic method is not so reliable, and it needs to be modified. Then there is for

instance no guarantee that it includes the viscosity solution among its branches.

In [9], Benamou introduced a more natural decomposition of the computational domain, which ensures that all phases in the multibranch solution are captured. In his method, the domain is cut along caustic curves. The caustics are detected by solving an accompanying PDE that enables a continuous monitoring of the geometrical spreading. The geometrical spreading vanishes at caustics, which therefore can be found numerically by checking sign changes in the computed geometrical spreading. See also [12, 86].

3.3 Wave front methods

Wave front methods are closely related to standard ray tracing, but instead of computing a sequence of individual rays, a wave front is evolved in physical or phase space. This can be based on the ODE formulation (2.12, 2.13) or the PDE formulation (2.31).

The propagation of a wave front in the xy-plane is given by the velocity $c(\boldsymbol{x})$ in its normal direction $\hat{\boldsymbol{n}}$. The velocity $\boldsymbol{u}=(u,v)$ of the wave front in the xy-plane is thus

$$(u,v)=c(\boldsymbol{x})\hat{\boldsymbol{n}}=c(\boldsymbol{x})\,(\cos\theta,\sin\theta), \tag{3.3}$$

where θ is the angle between the normal vector and the x-axis. At caustic and focus points, the normal direction is not defined, and front tracking methods based on (3.3) break down.

The tracing of the wavefronts in phase space facilitates problems including the formation of caustics, as is seen in the following simple example. In Fig. 13, left frame, an initial circular wave front is given in the xy-plane. This frame also displays the phase plane curve γ in $\mathbb{R}^3$ together with its $x\theta$-and $y\theta$-projections. Let the circular wave front contract with time in a constant medium, $c(\boldsymbol{x})\equiv 1$, and be focused to a point $(x,y)=(1,1)$ at time $t=1$. Although degenerate in the xy-plane, the representations of γ at $t=1$ in the $x\theta$- and $y\theta$-planes are smooth and the evolution as well as the computation of amplitudes can easily be continued to $t>1$.

Wave front construction is an ODE-based method that uses (2.12, 2.13). For the PDE-based wave front methods in phase space, the evolution of the front is given by the Liouville equation (2.31) and the front is represented by some interface propagation technique. We shall here discuss the application of the segment projection method, [28, 97], and also outline level set techniques, [74]. The segment projection method uses an explicit representation of the wave front while the level set method uses an implicit representation: see below.

3.3.1 Wave front construction

Wave front construction is a front tracking method in which Lagrangian markers on the phase space wave front is propagated according to the ray equations (2.14, 2.15). To maintain an accurate description of the front, new markers are adaptively inserted by interpolation when the resolution of the front deteriorates, *e.g.* in shadow zones. The method was introduced by Vinje et al in [104, 105].

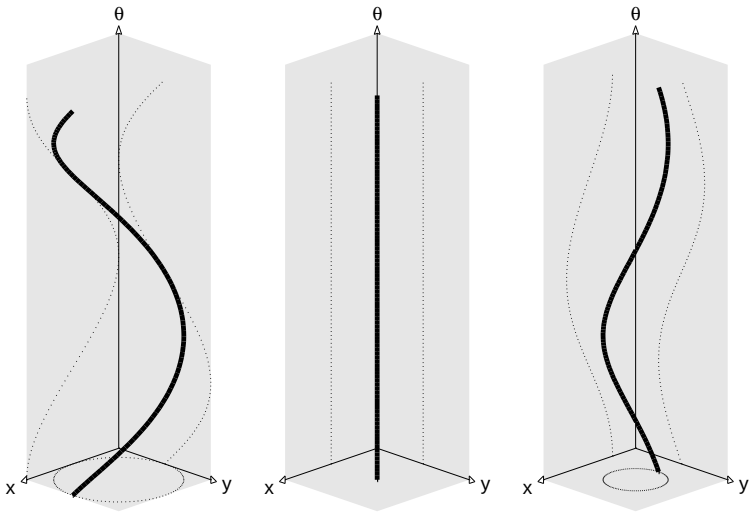

Figure 13: Phase plane curve γ: thick line, with projections onto xy-, $x\theta$- and $y\theta$-planes: dotted lines. The left frame shows the initial circular wave front at $t=0$. The middle frame shows the focus at $t=1$. The right frame shows the wave front after the focus at $t=1.5$.

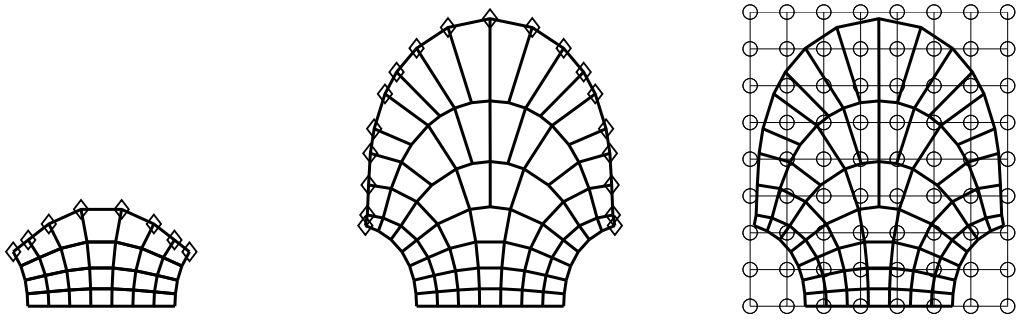

Figure 14: Wave front construction. Markers ($\diamond$) on the wave front are propagated as ordinary rays (left). Grid approximates the wave front in physical space, $\boldsymbol{x}(t,r)$ at constant t- and r-values. When the markers move too wide apart to accurately describe the front, new markers are inserted via interpolation (middle). The traveltimes and possibly amplitudes on the wave front are interpolated onto a regular grid as the front propagates (right).

Let us consider the two-dimensional case. As in Section 2.2 we assume that the wave front in phase space is described by $(\boldsymbol{x}(t,r),\boldsymbol{p}(t,r))$ at time t, where r is the parametrization induced by the parametrization of the source. The markers $(\boldsymbol{x}_j^n,\boldsymbol{p}_j^n)$ are initialized uniformly in r at $t=0$, $(\boldsymbol{x}_j^0,\boldsymbol{p}_j^0)=(\boldsymbol{x}(0,j\Delta r),\boldsymbol{p}(0,j\Delta r))$. Each marker is updated by a standard ODE-solver, such as a fourth order Runge-Kutta method, applied to the ray equations (2.14, 2.15). Thus the markers approximately trace rays, and

$$\boldsymbol{x}_j^n \approx \boldsymbol{x}(n\Delta t,j\Delta r), \qquad \boldsymbol{p}_j^n \approx \boldsymbol{p}(n\Delta t,j\Delta r), \qquad \forall n>0,j.$$

See Fig. 14 (left).

When the resolution of the wave front worsens, new markers must be inserted. The location in phase space of the new points is found via interpolation from the old points. A new marker $(\boldsymbol{x}^n_{j+1/2}, \boldsymbol{p}^n_{j+1/2})$ between markers j and $j+1$ would satisfy,

$$\boldsymbol{x}^n_{j+1/2} \approx \boldsymbol{x}(n\Delta t, j\Delta r + \Delta r/2), \qquad \boldsymbol{p}^n_{j+1/2} \approx \boldsymbol{p}(n\Delta t, j\Delta r + \Delta r/2).$$

See Fig. 14 (middle). When deciding on whether to add new markers, it is not sufficient only to look at the distance in physical space between the old markers, because it degenerates at caustics and focus points. The distance in the phase variable should also be taken into account, [88]. A useful criterion is to add a new marker between markers j and $j+1$ if

$$|\boldsymbol{x}^n_{j+1} - \boldsymbol{x}^n_j| \geq \text{TOL} \qquad \text{or} \qquad |\boldsymbol{p}^n_{j+1} - \boldsymbol{p}^n_j| \geq \text{TOL},$$

for some tolerance TOL. This criterion ensures that the phase wave front remains fairly uniformly sampled. Lambaré et al [57] introduced another criterion, where more points are added when the curvature of the phase space wave front is large. For each marker, they compute the additional quantities

$$\boldsymbol{X}^n_j \approx \boldsymbol{x}_r(n\Delta t, j\Delta r), \qquad \boldsymbol{P}^n_j \approx \boldsymbol{p}_r(n\Delta t, j\Delta r),$$

via the ODE system (2.28). Based on the fact that

$$\begin{aligned} &|\boldsymbol{x}(t, r+\Delta r) - \boldsymbol{x}(t,r) - \Delta r \boldsymbol{x}_r(t,r)| \approx \frac{1}{2}(\Delta r)^2 |\boldsymbol{x}_{rr}| \geq \frac{1}{2}(\Delta r |\boldsymbol{x}_r|)^2 \kappa(r) \\ \approx &\frac{1}{2}|\boldsymbol{x}(t, r+\Delta r) - \boldsymbol{x}(t,r)|^2 \kappa(r), \end{aligned}$$

where $\kappa(r)$ is the curvature, the criterion for adding a new marker is taken as

$$|\boldsymbol{x}^n_{j+1} - \boldsymbol{x}^n_j - \Delta r \boldsymbol{X}^n_j| \geq \text{TOL} \qquad \text{or} \qquad |\boldsymbol{p}^n_{j+1} - \boldsymbol{p}^n_j - \Delta r \boldsymbol{P}^n_j| \geq \text{TOL}.$$

The computed variables $\boldsymbol{X}^n_j$, which is proportional to the geometrical spreading, and $\boldsymbol{P}^n_j$ are also used for computing the amplitude and to simplify high order interpolation when inserting new markers, and in the grid interpolation below.

Finally, the interesting quantities carried by the markers on the wave front, such as traveltime and amplitude, are interpolated down on a regular cartesian grid, see Fig. 14 (right). The wave front construction covers the physical space by quadrilateral "ray cells." The interpolation step involves mapping the grid points to the right ray cells, in order to find the markers and marker positions from which to interpolate.

In three dimensions the wave front is a two-dimensional surface. The method generalizes by using a triangulated wave front, and performing the same steps as above. Interpolation can be done in essentially the same way as in two dimensions, but it is more complicated and the ray cells are now triangular prism-like "ray tubes." See *e.g.* [16].

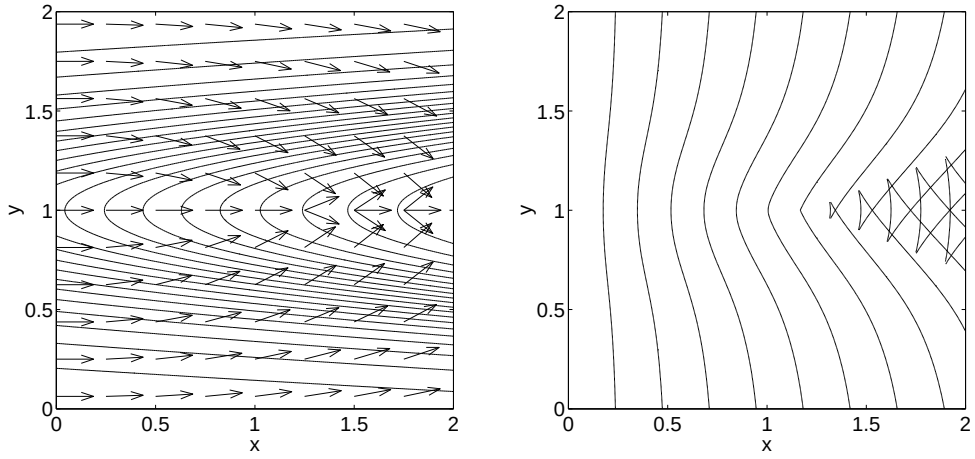

Figure 15: Results for the lens simulation. Left frame: local ray directions with contour lines of index of refraction overlayed; right frame: wave front in the xy-plane for a sequence of arrival times (T-values).

3.3.2 Segment projection method

The segment projection method is a PDE-based computational method for tracking the dynamic evolution of interfaces, [95, 96]. The basic idea is to represent a curve or surface as a union of segments. Each segment is chosen such that it can be given as a function of the independent variables. The representation is thus analogous to a manifold being defined by an atlas of charts. The motions of the individual segments are given by partial differential equations based on the physics describing the evolution of the interfaces. In the geometrical optics case the manifold is the Lagrangian submanifold in phase space mentioned in Section 2.2 and the motion is governed by (2.23, 2.24, 2.25).

Let us consider a two-dimensional case such as the one in Fig. 15, where a plane wave is refracted by a smooth lens. Initial data is given on the source line $x=0$. In this case the x-axis can be used as evolution direction. More precisely, we start from (2.23, 2.24, 2.25) and assume that there are no turning rays, *i.e.* there is a constant C such that $|\theta| \le C < \pi/2$ for all times. Time is then not explicitly needed in the calculation and θ, y and ϕ can be computed as a function of x (and initial position y_0) directly. The travel time T (which is also the phase ϕ) must be computed by a separate ODE. Dividing (2.24, 2.25) and inverting (2.23), we get

$$\begin{aligned} &\frac{d}{dx}\begin{pmatrix} y \\ \theta \end{pmatrix} = \begin{pmatrix} \tan\theta \\ \eta^{-1}(\eta_y - \eta_x \tan\theta) \end{pmatrix} =: \boldsymbol{u}(y,\theta), \\ &\frac{dT}{dx} = \frac{\eta}{\cos\theta}, \\ &y(0,y_0) = y_0, \quad \theta(0,y_0) = 0, \quad T(0,y_0) = 0. \end{aligned} \tag{3.4}$$

This is sometimes called a *paraxial approximation* of the geometrical optics equations.

A reduced description of the Lagrangian submanifold is given by $(x, y(x,y_0), \theta(x,y_0))$.

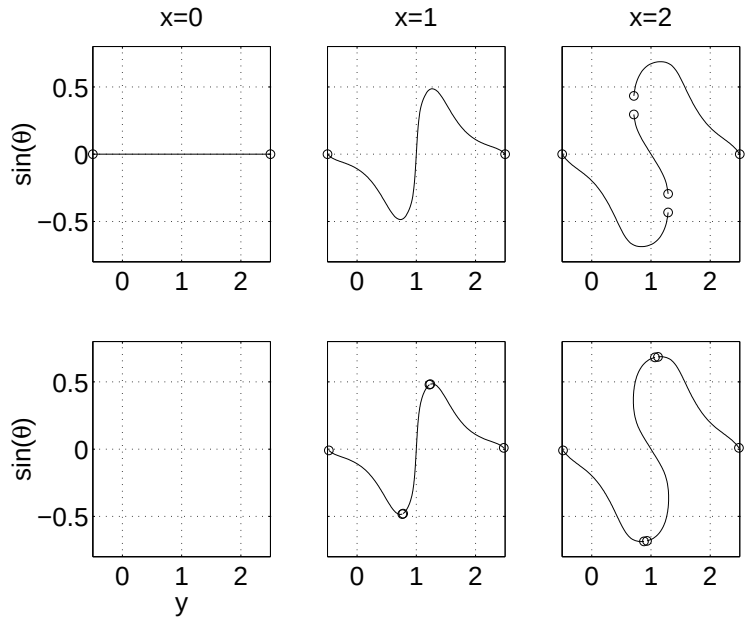

Figure 16: Segment structure for lens simulation corresponding to phase plane curve in Fig. 15. Upper row: y-segments; lower row: θ-segments.

Since caustics in general develop, the curve $\gamma(x) = \{(y(x,y_0),\theta(x,y_0)) \,:\, y_0 \in \mathbb{R}\}$ is not globally the graph of a function, for fixed x. Instead it will be represented by θ- and y-segments, given by the functions $Y_j(x,\theta)$ and $\Theta_k(x,y)$ respectively. The domains of the independent variables of these functions are projections of the segments onto the coordinate axis. For fixed x, the coordinates of the points on γ are given by $(y,\theta) = (Y_j(x,\theta),\theta)$ or $(y,\theta) = (y,\Theta_k(x,y))$. For each point on γ, there is at least one segment defining the curve. To make the description complete, information about the connectivity of segments must also be provided. For each segment in one variable there is information regarding which parts of the curve has overlap with segments in the other variable, as well as pointers to these segments.

The number of segments needed to describe a curve depends on the shape of the curve. An extremum of a function $Y_j(x,\theta)$ in θ defines a separation point for the y-segments, as no segment given as a function of y can continue past this point. Similarly, an extremum in y of a function $\Theta_k(x,y)$ defines a separation point for the θ-segments. A sketch of a distribution of segments is shown in Fig. 16 for various values of x. Note that the separation points for the y-segments correspond to caustic points.

The curve is moved by the velocity field $\boldsymbol{u} = (u,v)$ in (3.4). Let $\bar{y}(x)$ and $\bar{\theta}(x)$ solve the ODE in (3.4). Then

$$u = \frac{d}{dx} Y(x,\bar{\theta}(x)) = Y_x + \bar{\theta}_x Y_y = Y_x + v Y_\theta,$$

and similarly for $\Theta(x,\bar{y}(x))$. Hence, we get evolutionary partial differential equations for

the segments $\Theta(x,y)$ and $Y(x,\theta)$,

$$\frac{\partial Y}{\partial x}+v\frac{\partial Y}{\partial \theta}=u, \qquad \frac{\partial \Theta}{\partial x}+u\frac{\partial \Theta}{\partial y}=v.$$

After each numerical advection step, the segment representation is re-initialized. Dynamic creation and elimination of segments is employed to follow the evolution of the curves. New segments are created if necessary, and segments are removed when they are no longer needed. The connectivity of segments must be kept updated in such a way that the pointers relating segments represent the current configuration. For example, at $x=2$ in Fig. 16 (third column) a new maximum and minimum have appeared in the middle θ-segment. The number of y-segments is then increased, as is seen in the figure.

The travel time, T, is a quantity defined on the phase plane curve γ. Let T^y and T^θ be the traveltime associated to y- and θ-segments respectively. As above, the chain rule gives

$$\frac{\eta}{\cos\theta}=\frac{d}{dx}T^y(x,\bar\theta(x))=T^y_x+\bar\theta_x T^y_\theta=T^y_x+vT^y_\theta,$$

and again, similar for T^θ. This yields the following travel time differential equations, defined for the y-segments and θ-segments,

$$\frac{\partial T^y}{\partial x}+u\frac{\partial T^y}{\partial y}=\frac{\eta(x,y)}{\cos\theta}, \qquad \frac{\partial T^\theta}{\partial x}+v\frac{\partial T^\theta}{\partial \theta}=\frac{\eta(x,y)}{\cos\theta}. \tag{3.5}$$

The amplitude can be computed in the same way as the travel time T by solving for two unknowns on the curve corresponding to the quantities in (2.28).

3.3.3 Level set methods

The level set method was introduced by Osher and Sethian in [74] as a general technique for the simulation of moving interfaces. Level set methods for special applications had been introduced earlier. It uses an implicit representation of an interface in $\mathbb{R}^d$ as the zero level set of a function $\phi(t,\boldsymbol{x})$. The motion of the interface following a velocity field $\boldsymbol{u}(t,\boldsymbol{x})$ is given by a PDE for the level set function ϕ,

$$\phi_t+\boldsymbol{u}\cdot\nabla\phi=0. \tag{3.6}$$

This technique has been successfully applied to many different types of problems. Examples are multiphase flow, etching, epitaxial growth, image processing and visualization, described in the books [73, 84]. An attractive property is that equation (3.6) can be applied without modifications even if the topology of the interface changes as, for example, when merging occurs in multiphase flow.

For the location of the interface to be well defined, the gradient of ϕ in the direction normal to the interface should be bounded away from zero. In practice, the level set function ϕ is reinitialized at regular time intervals, such that it is approximately a signed distance function to the interface.

If $\phi(t,\boldsymbol{x})=0$ represents an evolving wave front given by geometrical optics the velocity is $\boldsymbol{u}(t,\boldsymbol{x})=c(\boldsymbol{x})\hat{\boldsymbol{n}}(\boldsymbol{x})$ where $\hat{\boldsymbol{n}}$ is the normal vector at the interface, that is,

$$\hat{\boldsymbol{n}}(t,\boldsymbol{x})=\frac{\nabla\phi}{|\nabla\phi|}.$$

This results in the eikonal equation,

$$\phi_t+c(\boldsymbol{x})\hat{\boldsymbol{n}}\cdot\nabla\phi=\phi_t+c(\boldsymbol{x})|\nabla\phi|=0.$$

A direct application will thus clearly not satisfy the linear superposition principle. As was noted in [72] the method can, however, still be used if we approximate the wave front in phase space and evolve the front using the Liouville equation (2.31), similar to what was done in the segment projection method. The wave front in the kinetic formulation (2.31) is of higher codimension, and such geometrical objects must be represented by the intersection of interfaces that are given by different level set functions. In two dimensions, a wave front like the helix in Fig. 13 can be defined by the intersection of two regular surfaces. The evolution of both level set functions $\phi_i(t,x,y,\theta)$, with $i=1,2$, is defined by the same velocity vector given by (2.23, 2.24, 2.25). They thus satisfy a reduced form of the Liouville equation (2.31),

$$\partial_t\phi_i+c\cos\theta\partial_x\phi_i+c\sin\theta\partial_y\phi_i+(c_x\sin\theta-c_y\cos\theta)\partial_\theta\phi_i=0. \tag{3.7}$$

If the initial wave front is given as the zero level set of the function $\psi_0(x,y)$ then initial data for (3.7) can for instance be taken as

$$\phi_1(0,x,y,\theta)=\psi_0(x,y),\qquad \phi_2(0,x,y,\theta)=\sin\theta\partial_x\psi_0(x,y)-\cos\theta\partial_y\psi_0(x,y).$$

The methodology can be generalized to many other types of equations and to higher dimensions [20, 22, 47, 64, 77]. An extensive review can be found in [65].

A practical problem with this approach is that the evolution of the one dimensional object representing the wave front requires approximation of the evolution of two level set functions in three dimensions. For wave fronts in $\mathbb{R}^3$, three level set functions in five independent variables and time are required. The computational burden can be reduced by restricting the computation to a small neighborhood of the wave front. In order to have a well-functioning algorithm, a number of special techniques are useful. Reinitialization of the level set functions ϕ_i, $i=1,\cdots,d$ in d dimensions should be performed at regular time intervals, such that

$$|\nabla\phi_i|\approx 1,\qquad \nabla\phi_i\cdot\nabla\phi_j\approx 0,\quad i\neq j,$$

at the interface.

A method to compute amplitudes in the phase space level set framework was introduced in [45, 46]. Let $w(t,x,y,\theta)$ be the solution to the reduced Liouville equation (3.7) with initial data

$$w(0,x,y,\theta)=A_0(x,y)^2|\nabla\phi_1(0,x,y,\theta)\cdot\nabla\phi_2(0,x,y,\theta)^\perp|,$$

where $A_0(x,y)$ is the initial amplitude of the front, extended smoothly to be defined for all $(x,y)\in\mathbb{R}^2$. The function w is smooth, positive and bounded also at caustics. One can then show that the amplitude on the wavefront at later times can be obtained from

$$A^2(t,x,y)\delta_{\Gamma(t)}(x,y)=\int_0^{2\pi} w\delta(\phi_1)\delta(\phi_2)d\theta.$$

Here $\delta_{\Gamma(t)}$ is a delta function supported on the wavefront $\Gamma(t)$ at time t. The problem is thus reduced to the numerical approximation of integrals involving delta functions with level set functions as arguments. This is another current research field. See e.g. [29, 85, 98, 99].

Boundaries can be treated in the level set framework by having the boundary coincide with the grid boundary in physical space, and applying suitable conditions, e.g. reflection boundary conditions, see [21]. For interfaces where the wave speed is discontinuous, it is in practice difficult to have the grid aligned with the interface. Instead one would like to have methods that automatically capture the interface effect using regular grids. The behavior of the solution at an interface is, however, not uniquely defined by the geometrical optics equations, which in the level set form are linear equations like (3.7) with discontinuous ($c(x,y)$) and even delta-type ($c_x(x,y)$, $c_y(x,y)$) coefficients. Additional conditions given by the physics of the problem must be incorporated, *cf.* Section 2.4. Moreover, any standard method using a direct discretization across a discontinuity and explicit time stepping would have a very severe CFL condition because of the c_x and c_y terms in the equation. These problems were solved in [48, 49] by constructing a certain Hamiltonian-preserving numerical flux, where the physically relevant interface conditions can be included at the interfaces. The resulting Hamiltonian-preserving explicit schemes are proved to be stable, positive and contractive under mild assumptions on the initial data and a CFL condition which is only constrained by the size of the coefficients in the smooth regions.

3.4 Moment-based methods

Moment-based methods take as their starting point the kinetic formulation of geometrical optics,

$$f_t+\frac{1}{\eta^2}\boldsymbol{p}\cdot\nabla_x f+\frac{1}{\eta}\nabla_x\eta\cdot\nabla_p f=0, \tag{3.8}$$

where $f(t,\boldsymbol{x},\boldsymbol{p})\geq 0$ is the density of particles in phase space. Like kinetic equations in general, solving the full equation (3.8) by direct numerical methods would be expensive, because of the large number of independent variables (six in 3D). (See, however, also Section 3.5 where this is done for a stationary version of (3.8).) Instead one can use the classic technique of approximating a kinetic transport equation set in high-dimensional phase space $(t,\boldsymbol{x},\boldsymbol{p})$, by a finite system of moment equations in the reduced space $(t,\boldsymbol{x})$. See, for instance, [39], and more recently [60]. In general the moment equations form a system of conservation laws that gives an approximation of the true solution. The

classical example is the compressible Euler approximation of the Boltzmann equation. In the geometrical optics setting, the moment system is, however, typically *exact* under the closure assumption that at most N rays cross at any given point in time and space. In fact, this moment system solution is equivalent to N disjoint pairs of eikonal and transport equations (2.6, 2.7) when the solution is smooth.

Brenier and Corrias, [14], originally proposed this approach for finding multivalued solutions to geometrical optics problems in the one-dimensional homogeneous case. It was subsequently adapted for two-dimensional inhomogeneous problems by Engquist and Runborg, [26, 81]. See also Gosse [35]. More recently, the same technique has been applied to the Schrödinger equation by Jin and Li [44], Gosse, Jin and Li [36], and Sparber, Markowich and Mauser [87].

Let us start by defining the moments m_{ij}, with $\boldsymbol{p}=(p_1,p_2)^T$, as

$$m_{ij}(t,\boldsymbol{x})=\frac{1}{\eta(\boldsymbol{x})^{i+j}}\int_{\mathbb{R}^2} p_1^i p_2^j f(t,\boldsymbol{x},\boldsymbol{p})d\boldsymbol{p}. \tag{3.9}$$

Next, multiply (3.8) by $\eta^{2-i-j}p_1^i p_2^j$ and integrate over $\mathbb{R}^2$ with respect to $\boldsymbol{p}$. After using integration by parts and assuming that f has compact support in $\boldsymbol{p}$, we see that formally m_{ij} will satisfy the infinite system of moment equations

$$(\eta^2 m_{ij})_t+(\eta m_{i+1,j})_x+(\eta m_{i,j+1})_y=i\eta_x m_{i-1,j}+j\eta_y m_{i,j-1}-(i+j)(\eta_x m_{i+1,j}+\eta_y m_{i,j+1}), \tag{3.10}$$

valid for all $i,j\geq 0$. For uniformity in notation we have defined $m_{i,-1}=m_{-1,i}=0,\forall i$. The system (3.10) is not closed. If truncated at finite i and j, there are more unknowns than equations. To close the system we have to make specific assumptions on the form of the density function f.

3.4.1 Closure with delta functions

We first consider the case when f is a weighted sum of delta functions in $\boldsymbol{p}$,

$$f(t,\boldsymbol{x},\boldsymbol{p})=\sum_{n=1}^{N} g_n\cdot\delta(\boldsymbol{p}-\boldsymbol{p}_n),\qquad \boldsymbol{p}_n=\eta\begin{pmatrix}\cos\theta_n\\ \sin\theta_n\end{pmatrix}. \tag{3.11}$$

Hence, for fixed values of $\boldsymbol{x}$ and t, the particle density f is non zero at a maximum of N points, and only when $|\boldsymbol{p}|=\eta(\boldsymbol{x})$. This form of f is motivated by (2.34). If the wave equation solution has the form

$$u(t,x)\approx\sum_{n=1}^{N} A_n(t,\boldsymbol{x})e^{i\omega\phi_n(t,\boldsymbol{x})},$$

with smooth A_n and ϕ_n, then the new variables introduced here would be identified as $g_n=A_n^2$ and $\boldsymbol{p}_n=\nabla\phi_n$. Hence, the assumptions in (3.11) is that there are at most N crossing

rays at each point in space and time, with $g_n = g_n(t,\boldsymbol{x})$ being the intensity (particle density) of ray n and $\theta_n = \theta_n(t,\boldsymbol{x})$ its local direction.

A system describing N phases needs $2N$ equations, corresponding to the $2N$ unknowns g_k and θ_k. It turns out that a good choice of equations are the ones for the moments $m_{2\ell-1,0}$ and $m_{0,2\ell-1}$ with $\ell = 1,\cdots,N$,

$$\begin{aligned}(\eta^2 m_{2\ell-1,0})_t + (\eta m_{2\ell,0})_x + (\eta m_{2\ell-1,1})_y &= (2\ell-1)(\eta_x m_{2\ell-2,0} - \eta_x m_{2\ell,0} - \eta_y m_{2\ell-1,1}),\\ (\eta^2 m_{0,2\ell-1})_t + (\eta m_{1,2\ell-1})_x + (\eta m_{0,2\ell})_y &= (2\ell-1)(\eta_y m_{0,2\ell-2} - \eta_x m_{1,2\ell-1} - \eta_y m_{0,2\ell}).\end{aligned} \tag{3.12}$$

We collect those moments in a vector,

$$\boldsymbol{m} = (m_{10}, m_{01}, m_{30}, m_{03}, \cdots, m_{2N-1,0}, m_{0,2N-1})^T. \tag{3.13}$$

Inserting (3.11) into the definition of the moments (3.9) yields

$$m_{ij} = \sum_{n=1}^{N} g_n \cos^i\theta_n \sin^j\theta_n. \tag{3.14}$$

We also introduce new variables,

$$\boldsymbol{u}_n = g_n \begin{pmatrix}\cos\theta_n\\ \sin\theta_n\end{pmatrix}, \qquad \boldsymbol{u} = \begin{pmatrix}\boldsymbol{u}_1\\ \vdots\\ \boldsymbol{u}_N\end{pmatrix} \in \mathbb{R}^{2N}, \tag{3.15}$$

where $\boldsymbol{u}_n$ thus shows the direction and strength of ray n. Clearly, each moment defined in (3.14) depend on $\boldsymbol{u}$ in a straightforward way, $m_{ij} = m_{ij}(\boldsymbol{u})$. In particular, one can define a function $\boldsymbol{F}_0 : \mathbb{R}^{2N} \to \mathbb{R}^{2N}$ through the equation

$$\boldsymbol{F}_0(\boldsymbol{u}) = \boldsymbol{m}. \tag{3.16}$$

Similarly, we define the functions $\boldsymbol{F}_1(\boldsymbol{u})$, $\boldsymbol{F}_2(\boldsymbol{u})$ and $\boldsymbol{K}(\boldsymbol{u},\eta_x,\eta_y)$, for the remaining columns in (3.12). This permits us to write (3.12) as a system of nonlinear conservation laws with source terms

$$(\eta^2\boldsymbol{m})_t + \boldsymbol{F}_1 \circ \boldsymbol{F}_0^{-1}(\eta\boldsymbol{m})_x + \boldsymbol{F}_2 \circ \boldsymbol{F}_0^{-1}(\eta\boldsymbol{m})_y = \boldsymbol{K}(\boldsymbol{F}_0^{-1}(\boldsymbol{m}),\eta_x,\eta_y). \tag{3.17}$$

The functions $\boldsymbol{F}_j$ and $\boldsymbol{K}$ are rather complicated nonlinear functions. In the most simple case, $N = 1$, the function $\boldsymbol{F}_0$ is the identity, and

$$\boldsymbol{F}_1 = \frac{u_1}{|\boldsymbol{u}|}\begin{pmatrix}u_1\\ u_2\end{pmatrix}, \quad \boldsymbol{F}_2 = \frac{u_2}{|\boldsymbol{u}|}\begin{pmatrix}u_1\\ u_2\end{pmatrix}, \quad \boldsymbol{K} = \frac{\eta_x u_2 - \eta_y u_1}{|\boldsymbol{u}|}\begin{pmatrix}u_2\\ -u_1\end{pmatrix}.$$

For $N = 2$, let $\boldsymbol{w} = (w_1, w_2)^T$ and

$$f_0 = \begin{pmatrix}w_1\\ w_2\\ w_1^3/|\boldsymbol{w}|^2\\ w_2^3/|\boldsymbol{w}|^2\end{pmatrix}, \qquad f_1 = \frac{w_1}{|\boldsymbol{w}|}f_0, \qquad f_2 = \frac{w_2}{|\boldsymbol{w}|}f_0.$$

Then $\boldsymbol{F}_j = \boldsymbol{f}_j(u_1,u_2)+\boldsymbol{f}_j(u_3,u_4)$ for $j=0,1,2$. Note that the functions $\boldsymbol{F}_j$ are not invertible; the vectors $\boldsymbol{u}_n$ can for instance be permutated without changing the value of the moments. The compositions with $\boldsymbol{F}_0^{-1}$, *e.g.* $\boldsymbol{F}_1\circ\boldsymbol{F}_0^{-1}$, can, however, be shown to be well-defined and continuous [81] for almost all $\boldsymbol{m}$. This means that the system (3.17) is essentially closed. This would in general not be true if we had made another choice of moments in (3.12).

Analysis of the conservation laws

The main advantage with the moment-based methods is that the multiple phase systems possess a *finite superposition principle* in the following sense. If the moments corresponding to $\boldsymbol{u}_n$, $n=1,\cdots,N$ are N solutions to the single phase system, then the moments corresponding to $\boldsymbol{u}=(\boldsymbol{u}_1,\cdots,\boldsymbol{u}_N)^T$ is a solution to the N-phase system. This follows from a trivial computation if the solutions are smooth. Physical solutions can, however, have discontinuities in g. If weak solutions are introduced, one can show that a sufficient condition for the superposition principle to hold is just that g is bounded and that θ is continuous and has locally bounded variation [81]. (A discontinuous θ would typically not be physical.)

A distinguishing feature of the system (3.17) is that it typically has measure solutions of delta function type, even for smooth and compactly supported initial data. These appear when the physically correct solution passes outside the class of solutions that the system (3.17) describes. If initial data dictate a physical solution with M phases for $t>T$, the system (3.17) with $N<M$ phases will have a measure solution for $t>T$, *cf.* Fig. 17(a).

In [26] it was shown that the general system (3.17) is nonstrictly hyperbolic for all states $\boldsymbol{m}$ and N. The same was shown for the Schrödinger equation case in [44]. The Jacobian has a Jordan-type degeneracy and there will never be more than N linearly independent eigenvectors for the $2N\times 2N$ system. The systems are thus not well posed in the strong sense, which is reflected in their sensitivity to numerical treatment. Even for smooth problems, many standard numerical schemes converge poorly in L^1 and may fail to converge in L^∞, [26, 80]. Kinetic schemes have been recognized to better handle nonstrictly hyperbolic problems. They were used with success in [36, 44]. Also note that in heterogeneous media the source term may be very stiff because of large gradients in the index of refraction. It is therefore important to treat it correctly, for example by using so-called well-balanced schemes, [35, 36].

Another numerical difficulty is to evaluate the flux functions $\boldsymbol{F}_1\circ\boldsymbol{F}_0^{-1}$ and $\boldsymbol{F}_2\circ\boldsymbol{F}_0^{-1}$ and the source function $\boldsymbol{K}$. It is necessary to solve a nonlinear system of equations

$$\boldsymbol{F}_0(\boldsymbol{u})=\boldsymbol{m}, \tag{3.18}$$

for each time step, at each grid point. Solving (3.18) can be difficult. When $N=1,2$ there is an analytical way to invert $\boldsymbol{F}_0$: see [81]. For $N>2$ an iterative solver must be used.

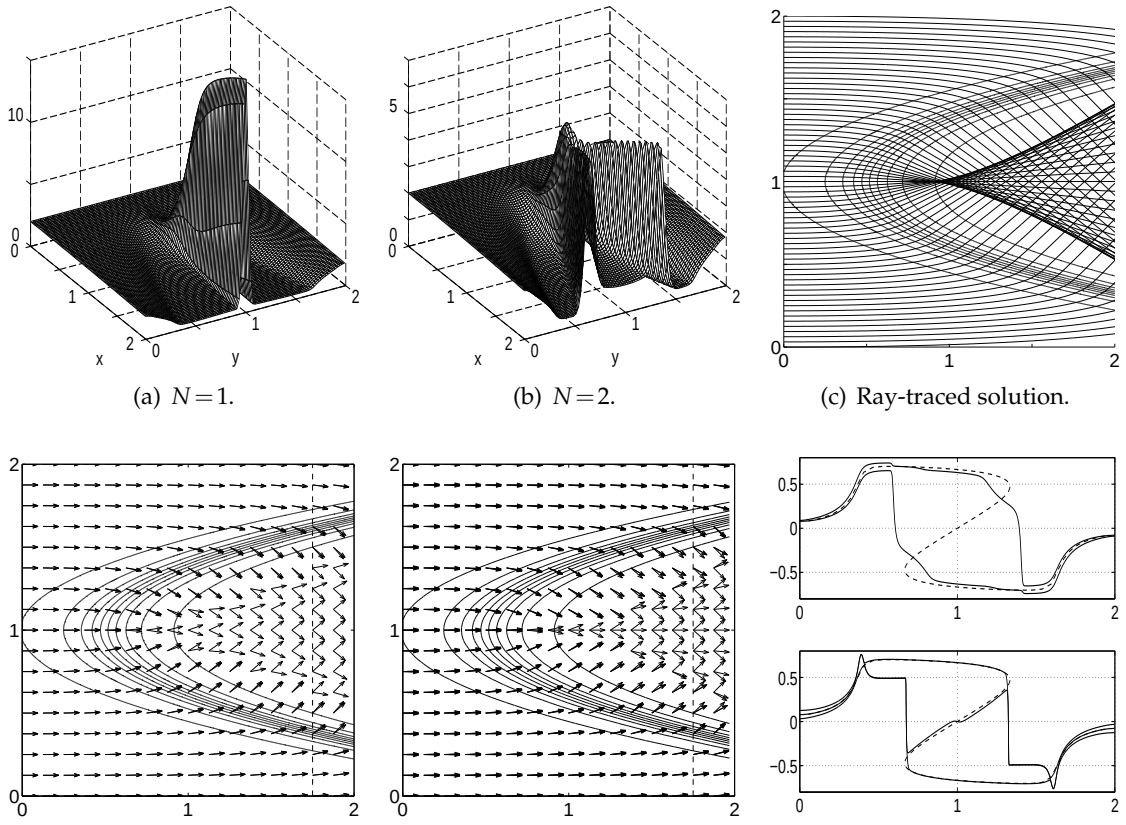

(a) $N=1$. (b) $N=2$. (c) Ray-traced solution.

(d) δ-equations, $N=2$. (e) H-equations, $N=3$. (f) δ-equations, $N=2$ (above), H-equations, $N=3$ (below).

Figure 17: *Wedge*. Amplitude results (top row) for δ-equations with $N=1$, 2. Top left and top middle pictures show total ray strength, *i.e.* g and g_1+g_2 respectively. Top right figure shows a ray-traced solution with contour lines of the index of refraction superimposed. Lower left and lower middle figures show quiver plots of ray angles for δ- and H-equations with $N=2$, 3. A contour plot of the index of refraction is overlaid on the solutions. Lower right figure shows sine of ray angles (solid) in a cut at $x=1.75$ together with the corresponding values for a ray traced solution (dashed).

3.4.2 Closure with Heaviside functions

We can also consider a different form of f to close (3.10). By assuming that

$$f(t,\boldsymbol{x},\boldsymbol{p})=\frac{1}{\eta}\delta(|\boldsymbol{p}|-\eta)\sum_{n=1}^{N}(-1)^{n+1}H(\theta-\theta_n),\qquad \boldsymbol{p}=|\boldsymbol{p}|\begin{pmatrix}\cos\theta\\ \sin\theta\end{pmatrix}, \tag{3.19}$$

one can discard the amplitude information carried by g_n used in the previous section and only solve for the angles θ_n. In this way one gets fewer and less singular equations.

For fixed $(t,\boldsymbol{x})$, the density function f is supported by a set of intervals on the sphere $\{|\boldsymbol{p}|=\eta\}$. The intervals correspond to fans of rays whose edges are given by the unknown angles θ_n. The transport equation (3.8) governs the propagation of all these rays, and in

particular the rays at the edges, which will propagate just like ordinary rays as long as f stays of the form (3.19). The values of the N angles θ_n will then coincide with those of a problem with N rays crossing at each point, as long as the assumption (3.19) holds.

For this case we usually make the paraxial approximation mentioned in Section 3.3.2 and choose the equations for the moments $\{m_{0,\ell}\}$ with $\ell=0,\cdots,N-1$. The assumption (3.19) then leads to a steady state version of (3.10),

$$(\eta m_{1,\ell})_x+(\eta m_{0,\ell+1})_y=\ell(\eta_y m_{0,\ell-1}-\eta_x m_{1,\ell}-\eta_y m_{0,\ell+1}),\qquad \ell=0,\cdots,N-1. \tag{3.20}$$

This system is strictly hyperbolic as long as $\theta_n\neq\theta_\ell$ for all n,ℓ. Moreover, the same superposition principle as for the delta equations in Section 3.4.1 holds also for these Heaviside equations. Numerical schemes are not as sensitive as for the δ-equations. The evaluation of the flux functions is also easier; it was recently shown that the inversion corresponding to $\boldsymbol{F}_0(\boldsymbol{u})=\boldsymbol{m}$ can be reduced to a generalized eigenvalue problem $A\boldsymbol{x}=\lambda B\boldsymbol{x}$ for $A,B\in\mathbb{R}^{N\times N}$, which can be solved in a stable way with the QZ-algorithm, [37, 38]. Initialization of physically irrelevant phases is, however, more difficult for these equations. See [35, 81] for further discussion of the theory of this system and how to couple it with equations for the amplitudes.

3.4.3 Numerical example

We consider a problem where a plane wave, injected at $x=0$ with $\theta(0,y)=0$ and $g(0,y)=2$, is refracted by a smooth wedge similar to the one in Fig. 15. When the wave is refracted in the interface a second and third phase appear. A caustic develops around the point $(1,1)$, fanning out to the right: see Fig. 17(c).

The equations closed with delta and Heaviside functions (δ- and H-equations, in short) were solved in the square $[0,2]\times[0,2]$. Different aspects of the solutions are shown in Fig. 17. The δ-equations with $N=1$ only capture one of the phases, as expected. A delta function appear where rays try to cross. The $N=2$ system captures both the second phase and the caustic quite well. The H-equations cannot correctly capture the second phase when $N=2$. However, when $N=3$ all three phases are captured.

3.5 Full phase space methods

As was discussed in the introduction of this section, solving the full phase space Liouville equation (3.8) is significantly more expensive than solving *e.g.* the eikonal and transport equation. This is, however, only under the assumption that we are interested in the solution for just *one* set of initial data. In many applications, we seek instead the solution for *many* different initial data (sources), with the same index of refraction $\eta(\boldsymbol{x})$. Examples include the inverse problem in geophysics and the computation of radar cross sections. For these cases, solving a PDE in the full phase space can be an attractive alternative.

To describe the evolution in phase space we introduce the phase map (solution operator) $\mathcal{G}_t:\mathbb{R}^{2d}\to\mathbb{R}^{2d}$, mapping a ray's starting point $\boldsymbol{y}_0=(\boldsymbol{x}_0,\boldsymbol{p}_0)$ in phase space to its

location after time t. More precisely,

$$\mathcal{G}_t(\boldsymbol{y}_0)=\boldsymbol{y}(t),$$

when $\boldsymbol{y}(t)=(\boldsymbol{x}(t),\boldsymbol{p}(t))$ solves the ray equations (2.14, 2.15) with initial data $\boldsymbol{y}_0$.

3.5.1 Fast phase space method

The fast phase space method was put forth by Fomel and Sethian in [31]. They consider the unknown $\hat{\boldsymbol{y}}(\boldsymbol{x},\boldsymbol{p})$, defined in a subdomain Ω of phase space as the point where a bicharacteristic originating in $(\boldsymbol{x},\boldsymbol{p})\in\Omega$ first crosses the boundary $\partial\Omega$. Hence, in the phase map notation,

$$\hat{\boldsymbol{y}}(\boldsymbol{x},\boldsymbol{p})=\mathcal{G}_{T(\boldsymbol{x},\boldsymbol{p})}(\boldsymbol{x},\boldsymbol{p}),\qquad T(\boldsymbol{x},\boldsymbol{p})=\min_t\{t\geq 0\mid \mathcal{G}_t(\boldsymbol{x},\boldsymbol{p})\in\partial\Omega\}.$$

Then $\hat{\boldsymbol{y}}$ solves the *escape* equation

$$\begin{aligned} &D_x\hat{\boldsymbol{y}}\,\boldsymbol{p}+\eta D_p\hat{\boldsymbol{y}}\,\nabla\eta=0, && (\boldsymbol{x},\boldsymbol{p})\in\Omega,\\ &\hat{\boldsymbol{y}}(\boldsymbol{x},\boldsymbol{p})=(\boldsymbol{x},\boldsymbol{p}), && (\boldsymbol{x},\boldsymbol{p})\in\partial\tilde{\Omega}, \end{aligned} \tag{3.21}$$

where $D_x\hat{\boldsymbol{y}}$, $D_p\hat{\boldsymbol{y}}$ are the Jacobians of $\hat{\boldsymbol{y}}$ with respect to $\boldsymbol{x}$, $\boldsymbol{p}$ respectively and $\partial\tilde{\Omega}$ is the part of $\partial\Omega$ with ingoing characteristics. The escape equation can be derived by noting that $\hat{\boldsymbol{y}}(\boldsymbol{x}(t),\boldsymbol{p}(t))$ is constant along a bicharacteristic $(\boldsymbol{x}(t),\boldsymbol{p}(t))$. Therefore, after differentiation with respect to t and multiplication by η^2, the chain rule together with the ray equations (2.14, 2.15) give (3.21). Note that this is the stationary version of (3.8) with the scalar density function f replaced by the vector $\hat{\boldsymbol{y}}$. There is also an accompanying transport equation for the travel time $T(\boldsymbol{x},\boldsymbol{p})$ defined above, which represents the time it takes for a bicharacteristic starting at the point $(\boldsymbol{x},\boldsymbol{p})$ to reach the boundary. Since $\partial_t T(\boldsymbol{x}(t),\boldsymbol{p}(t))=1$, we get

$$\begin{aligned} &\boldsymbol{p}\cdot\nabla_x T+\eta\nabla\eta\cdot\nabla_p T=\eta^2, && (\boldsymbol{x},\boldsymbol{p})\in\Omega,\\ &T(\boldsymbol{x},\boldsymbol{p})=0, && (\boldsymbol{x},\boldsymbol{p})\in\partial\tilde{\Omega}. \end{aligned} \tag{3.22}$$

Both (3.21) and (3.22) are solved numerically by the fast marching method (see Section 3.2.1) adapted to the linear phase space setting. It is done in a Eulerian framework, on a fixed grid. In two dimensions, the phase space is three-dimensional, and the cost for fast marching is $\mathcal{O}(N^3\log N)$ when each dimensions is discretized with N grid points. The corresponding cost for three-dimensional problems is $\mathcal{O}(N^5\log N)$. The *slowness matching method* of Symes, [89,90], has a slightly different setting, but it can be seen as a method to solve (3.21, 3.22) in a subdomain of phase space where there are no turning rays, so that the paraxial approximation can be used (*cf.* Section 3.3.2). It has a comparable complexity.

The solution to (3.21, 3.22) gives the travel time to the boundary and escape location for rays with all possible starting points and starting directions in the domain Ω. The

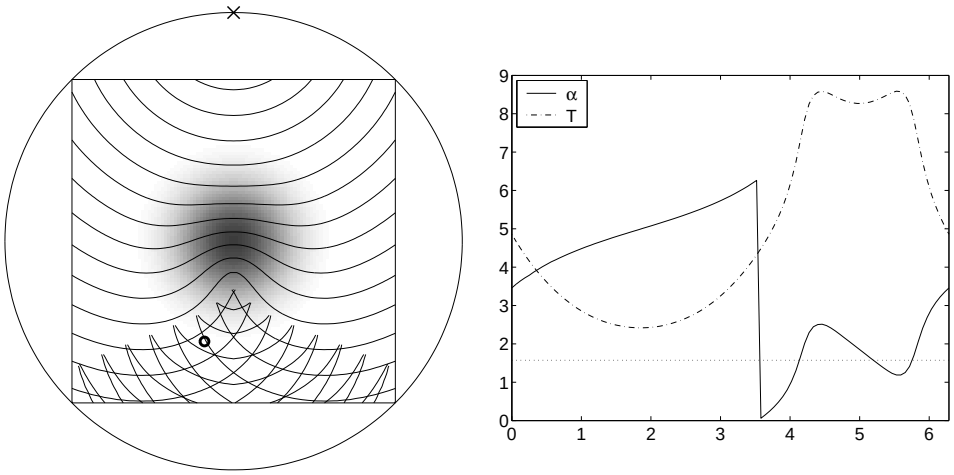

Figure 18: Travel time from a point source on the boundary $\partial\Omega$, marked "$\times$". Left frame: Isotime lines in a square part of Ω, with gray scale of index of refraction superimposed. Right frame: Plot of $\hat{x}(x_0,p)$ and $T(x_0,p)$ for a fixed point x_0, marked "$\circ$" in the left frame. Here, both $\hat{x}$ and p are one-dimensional periodic variables and represented by an angle $\alpha\in[0,2\pi)$. The source is located at $\hat{x}=x_1=\pi/2$ (dotted line in right frame). There are three solutions to (3.24) representing three different traveltimes. (The artificial solution introduced by the periodicity of $\hat{x}$ is discarded.)

travel times between any two points x_0 and x_1 can then be computed from the solution. First, solve

$$\hat{y}(x_0,p_0)=\hat{y}(x_1,p_1), \tag{3.23}$$

for p_0 and p_1. Then the travel time is $|T(x_0,p_0)-T(x_0,p_1)|$. There may be multiple solutions to (3.23), giving multiple travel times. If $x_1\in\partial\Omega$, the expression simplifies. Setting $\hat{y}=(\hat{x},\hat{p})$, we can solve

$$\hat{x}(x_0,p)=x_1, \tag{3.24}$$

for p to get the travel time $T(x_0,p)$. An example is shown in Fig. 18. To find the travel time at x_0 of a wave front that starts at the boundary of Ω in physical space, one instead needs to find p such that

$$\hat{p}(x_0,p)=\eta\hat{n}(\hat{x}(x_0,p)),$$

where $\hat{n}(\hat{x})$ is the normal of the boundary at $\hat{x}$. Again, the travel time is $T(x_0,p)$.

The amplitude can also be obtained directly through post-processing of the solution. Let us consider a point source at x_0 in two dimensions. In the notation of Section 2.2, we have

$$|A(\tilde{x}(t,r))|^{-2}\sim|\tilde{x}_r(t,r)|\eta(\tilde{x}(t,r)),$$

after assuming that $x_0(r)=x_0+\varepsilon(\cos r,\sin r)$ and $\varepsilon\to 0$. Set $p_0(r)=\eta(x_0)(\cos r,\sin r)^T$. Then there is a function $t(r)$ such that $\hat{x}(x_0,p_0(r))=\tilde{x}(t(r),r)$, and, after differentiation with respect to r,

$$D_p\hat{x}\,p_0^{\perp}=\tilde{x}_t t'(r)+\tilde{x}_r.$$

But, $\hat{\boldsymbol{p}}(\boldsymbol{x}_0,\boldsymbol{p}_0) \parallel \tilde{\boldsymbol{x}}_t \perp \tilde{\boldsymbol{x}}_r$ and since $|\hat{\boldsymbol{p}}| = \eta(\hat{\boldsymbol{x}})$,

$$|A(\hat{\boldsymbol{x}}(\boldsymbol{x}_0,\boldsymbol{p}_0))|^{-2} \sim \hat{\boldsymbol{p}}^{\perp} D_p \hat{\boldsymbol{x}}\, \boldsymbol{p}_0^{\perp}.$$

See also [71] for an adaptation of the fast phase space method to geodesics on a surface. This setting is e.g. relevant for computing the creeping ray contribution to radar cross sections.

3.5.2 Phase flow method

The phase flow method was proposed by Candès and Ying in [109]. Their idea is to compute an approximation of the whole phase map $\mathcal{G}_t$ on a grid. It can be seen as a clever tabulation of well chosen ray paths that allows for a rapid approximate evaluation of any other ray path. The method is in fact general and works for any autonomous ODE.

The key observation is the group property

$$\mathcal{G}_t(\mathcal{G}_s(\boldsymbol{y})) = \mathcal{G}_{t+s}(\boldsymbol{y}).$$

By induction, this leads to

$$\mathcal{G}_{n\Delta t}(\boldsymbol{y}) = \mathcal{G}_{n_0\Delta t}(\mathcal{G}_{n_1 2\Delta t}(\cdots \mathcal{G}_{n_k 2^k \Delta t}(\boldsymbol{y})\cdots)),$$

with n_j given by the binary expansion of n,

$$n = \sum_{j=0}^{k} n_j 2^j, \qquad n_j \in \{0,1\}.$$

Suppose we want to compute $\boldsymbol{y}(n\Delta t)$, with $n\Delta t \le T$, when the initial data is $\boldsymbol{y}_0$. Then $\boldsymbol{y}(n\Delta t) = \mathcal{G}_{n\Delta t}(\boldsymbol{y}_0)$ and if $\mathcal{G}_t$ can be applied at an $\mathcal{O}(1)$ cost, we can obtain $\boldsymbol{y}(n\Delta t)$ at an $\mathcal{O}(|\log \Delta t|)$ cost, since $k \le |\log_2(T/\Delta t)|$. Moreover, we only need to use $\mathcal{G}_{\Delta t}, \mathcal{G}_{2\Delta t}, \cdots, \mathcal{G}_{2^k\Delta t}$, i.e. $\mathcal{O}(|\log \Delta t|)$ instances of the phase map. In the phase flow method approximations of these instances are computed. One assumes[‡] that there is a compact submanifold $\mathcal{M}$ of phase space that is invariant under $\mathcal{G}_t$, i.e. if $\boldsymbol{y} \in \mathcal{M}$ then $\mathcal{G}_t(\boldsymbol{y}) \in \mathcal{M}$. One example would be when the coefficient $c(\boldsymbol{x})$ is periodic. The manifold is discretized with N grid points in each coordinate direction, such that $T/\Delta t \sim N$, and $\mathcal{G}_t$ is approximated by a grid function extended by interpolation to all of $\mathcal{M}$. The first instance, $\tilde{\mathcal{G}}_{\Delta t} \approx \mathcal{G}_{\Delta t}$, is computed by applying an ODE-solver to (2.14, 2.15) with each grid point $\tilde{\boldsymbol{y}}_0 \in \mathcal{M}$ as initial data. The remaining instances, $\tilde{\mathcal{G}}_t$ with $t = 2^j \Delta t$, are computed by repeated use of the recursion

$$\mathcal{G}_{2t}(\boldsymbol{y}) = \mathcal{G}_t(\mathcal{G}_t(\boldsymbol{y})),$$

plus interpolation. Local interpolation is used, so that applying $\tilde{\mathcal{G}}_t$ can be done in fixed time.

[‡]This is not a crucial assumption, and the method can be adapted also to other cases.

If the dimension of $\mathcal{M}$ is $2d-1$, the computational complexity is $\mathcal{O}(N^{2d-1}\log N)$ in time and memory to compute and store the approximations of the phase map instances. This is thus the same as the complexity for the fast phase space method. Once the phase map instances are computed, the cost to approximate $\boldsymbol{y}(n\Delta t)$, for any initial data, is only $\mathcal{O}(\log N)$. However, in practice one needs to take a few more instances of $\mathcal{G}_t$ than $O(|\log\Delta t|)$ because of stability issues when applying it many times. The stabilized method has a slightly worse complexity, $\mathcal{O}(N^{2d-1+s})$ for some small s.

To compute the amplitude one needs the derivative of the phase map. This can be computed in a way similar to $\mathcal{G}_t$ itself. Another possibility is to differentiate $\mathcal{G}_t$ numerically, as is done in the fast phase space method. The phase flow method has also been used to compute geodesics on surfaces [108].

3.6 Hybrid methods

We end this review by giving some brief comments on *hybrid* methods in which direct solvers of the wave equation are coupled with solvers based on one of the high frequency models. The high frequency approximation is bad where the wave length is relatively large compared to the scales on which the boundary or the index of refraction vary. One must then instead use an expensive, but accurate, direct solver. The main assumption in this section is that the parts where this is necessary, are small compared to the overall computational domain and that high frequency solvers are accurate in the remaining parts.

We confine the discussion to the scattering problem for the Helmholtz equation as in Section 2.6.1. This problem is often solved with hybrid methods in computational electromagnetics, see *e.g.* [43, 68, 92]. To fix ideas, let $\Omega\subset\mathbb{R}^3$ be a bounded open set representing the scatterer. We suppose furthermore that it has two disjoint, disconnected, components, $\Omega=\Omega_1\cup\Omega_2$ and $\Omega_1\cap\Omega_2=0$, where Ω_1 is small, $|\Omega_1|\sim\omega^{-1}$, and complicated, while Ω_2 is large, $|\Omega_2|\gg\omega^{-1}$, and smooth. Let u be the scattered field and u_{inc} the incident wave. Then

$$\begin{aligned}&\Delta u+\omega^2 u=0, && \boldsymbol{x}\in\mathbb{R}^3\setminus\overline{\Omega},\\ &u=-u_{\text{inc}}, && \boldsymbol{x}\in\partial\Omega,\end{aligned}$$

together with a radiation condition at infinity. Since Ω_2 is large, it is computationally very expensive to solve this problem completely with a direct solver.

As a first step to reduce the computational cost, one can use the *boundary decomposition method*, a common strategy for breaking up the problem into more tractable parts. It is an iterative method for u where the subscatterers Ω_1 and Ω_2 are treated independently in each iteration. The iterations start with u_j^0, $j=1,2$, the solutions to

$$\begin{aligned}&\Delta u_j^0+\omega^2 u_j^0=0, && \boldsymbol{x}\in\mathbb{R}^3\setminus\overline{\Omega}_j,\\ &u_j^0=-u_{\text{inc}}, && \boldsymbol{x}\in\partial\Omega_j.\end{aligned}$$

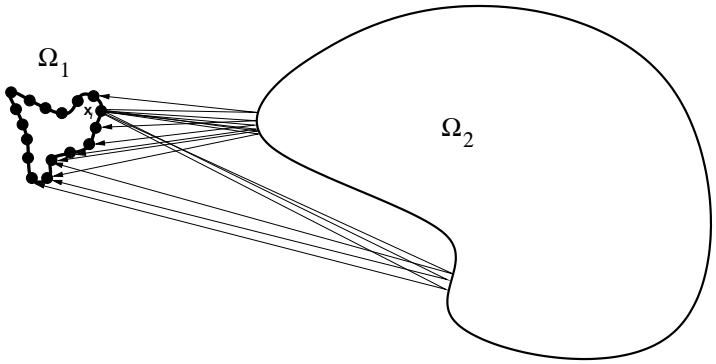

Figure 19: Interaction in one iteration between the subscatterers for the element at $\boldsymbol{x}_i$ on Ω_1. The element is assumed to radiate as a point source. Rays bouncing off Ω_2 and hitting the elements on Ω_1 are shown. Note that for some elements on Ω_1 there are multiple returning rays.

Then u_j^n is computed iteratively for $n=1,2,3,\cdots$, by solving

$$\begin{aligned} &\Delta u_j^n + \omega^2 u_j^n = 0, && \boldsymbol{x} \in \mathbb{R}^3 \setminus \overline{\Omega}_j, \\ &u_j^n = -u_{2-j}^{n-1}, && \boldsymbol{x} \in \partial\Omega_j. \end{aligned}$$

Note that the field from the other subscatterer, in the previous iteration, is used as boundary data. One can show that for disjoint subscatterers in $\mathbb{R}^3$ the iteration converges and

$$u = \sum_{n=0}^{\infty} u_1^n + u_2^n,$$

provided there is enough separation between the subscatterers [7]. The method easily generalizes to any finite number of subscatterers.

The idea with hybrid methods is to use a direct solver for the u_1^n problems that are set on the small Ω_1 subscatterer, and an approximate high-frequency solver for the u_2^n problems on the large Ω_2. The direct solver is usually a boundary element method, called *method of moments* in the computational electromagnetics community, [41]. The high frequency solver can be physical or geometrical optics, with or without the geometrical theory of diffraction extension. The coupling between the models is made by considering each surface element on the discretized Ω_1 subscatterer as a point source. For example, in the geometrical optics case, an element at $\boldsymbol{x}_i \in \Omega_1$ shoots out rays in all directions with a strength given by $u_1^n(\boldsymbol{x}_i)$. In order obtain the boundary conditions for u_1^{n+1} one has to find the rays that reflect off Ω_2 back to the elements on Ω_1, see Fig. 19.

Acknowledgments

To author would like to thank to Prof. Björn Engquist for many valuable discussions, as well as Debo Hu and Mohammad Motamed for providing Fig. 3(c) and Fig. 18, respectively.

References

[1] T. Abboud, J.-C. Nédélec and B. Zhou, Méthode des équations intégrales pour les hautes fréquences, C. R. Acad. Sci. Paris Sér. I Math., 318(2) (1994), 165-170.

[2] K. R. Aberegg and A. F. Peterson, Application of the integral equation asymptotic phase method to two-dimensional scattering, IEEE T. Antenn. Propag., 43 (1995), 534-537.

[3] R. Abgrall and J.-D. Benamou, Big ray tracing and eikonal solver on unstructured grids: Application to the computation of a multivalued traveltime field in the Marmousi model, Geophysics, 64 (1999), 230-239.

[4] V. I. Arnold, S. M. Gusein-Zade and A. N. Varchenko, Singularities of differentiable maps. Vol. I, in: Monographs in Mathematics, vol. 82, Birkhäuser Boston Inc., Boston, MA, 1985.

[5] V. M. Babich and V. S. Buldreyev, Asymptotic Methods in Short Wave Diffraction Problems, Moscow, Nauka, 1972 (In Russian); Springer, 1991 (English translation).

[6] G. Bal, G. Papanicolaou and L. Ryzhik, Radiative transport limit for the random Schrödinger equation, Nonlinearity, 15(2) (2002), 513-529.

[7] M. Balabane, Boundary decomposition for Helmholtz and Maxwell equations. I. Disjoint sub-scatterers. Asymptot. Anal., 38(1) (2004), 1-10.

[8] J.-D. Benamou, Big ray tracing: Multivalued travel time field computation using viscosity solutions of the eikonal equation, J. Comput. Phys., 128(4) (1996), 463-474.

[9] J.-D. Benamou, Direct computation of multivalued phase space solutions for Hamilton-Jacobi equations, Comm. Pure Appl. Math., 52(11) (1999), 1443-1475.

[10] J.-D. Benamou, An introduction to Eulerian geometrical optics (1992-2002), J. Sci. Comput., 19(1-3) (2003), 63-93.

[11] J.-D. Benamou, F. Castella, T. Katsaounis and B. Perthame, High frequency limit of the Helmholtz equations, Rev. Mat. Iberoamericana, 18(1) (2002), 187-209.

[12] J.-D. Benamou, O. Lafitte, R. Sentis and I. Solliec, A geometric optics based numerical method for high frequency electromagnetic fields computations near fold caustics - part I, J. Comput. Appl. Math., 156(1) (2003), 93-125.

[13] M. Boué and P. Dupuis, Markov chain approximations for deterministic control problems with affine dynamics and quadratic cost in the control, SIAM J. Numer. Anal., 36(3) (1999), 667-695.

[14] Y. Brenier and L. Corrias, A kinetic formulation for multibranch entropy solutions of scalar conservation laws, Ann. Inst. Henri Poincaré, 15(2) (1998), 169-190.

[15] O. P. Bruno, C. A. Geuzaine, J. A. Monro Jr. and F. Reitich, Prescribed error tolerances within fixed computational times for scattering problems of arbitrarily high frequency: the convex case, Philos. T. Roy. Soc. A, 362 (2004), 629-645.

[16] P. Bulant and L. Klimeš, Interpolation of ray theory traveltimes within ray cells, Geophys. J. Int., 139 (1999), 273-282.

[17] S. Cao and S. Greenhalgh, Finite-difference solution of the eikonal equation using an efficient, first-arrival, wavefront tracking scheme, Geophysics, 59(4) (1994), 632-643.

[18] F. Castella, B. Perthame and O. Runborg, High frequency limit of the Helmholtz equation II: Source on a general smooth manifold, Commun. Part. Diff. Eq., 27 (2002), 607-651.

[19] V. Červený, I. A. Molotkov and I. Psencik, Ray Methods in Seismology, Univ. Karlova Press, 1977.

[20] L.-T. Cheng, P. Burchard, B. Merriman and S. Osher, Motion of curves constrained on surfaces using a level-set approach, J. Comput. Phys., 175(2) (2002), 604-644.

[21] L.-T. Cheng, M. Kang, S. Osher, H. Shim and Y.-H. Tsai, Reflection in a level set framework

for geometric optics, CMES-Comp. Model. Eng. Sci., 5(4) (2004), 347-360.
[22] L.-T. Cheng, H. Liu and S. Osher, Computational high-frequency wave propagation using the level set method, with applications to the semi-classical limit of Schrödinger equations, Commun. Math. Sci., 1(3) (2003), 593-621.
[23] M. G. Crandall and P.-L. Lions, Viscosity solutions of Hamilton-Jacobi equations, Trans. Amer. Math. Soc., 277(1) (1983), 1-42.
[24] E. Darrigrand, Coupling of fast multipole method and microlocal discretization for the 3-D Helmholtz equation, J. Comput. Phys., 181(1) (2002), 126-154.
[25] J. J. Duistermaat, Oscillatory integrals, Lagrange immersions and unfolding of singularities, Commun. Pur. Appl. Math., 27 (1974), 207-281.
[26] B. Engquist and O. Runborg, Multiphase computations in geometrical optics, J. Comput. Appl. Math., 74 (1996), 175-192.
[27] B. Engquist and O. Runborg, Computational high frequency wave propagation, Acta Numerica, 12 (2003), 181-266.
[28] B. Engquist, O. Runborg and A.-K. Tornberg, High frequency wave propagation by the segment projection method, J. Comput. Phys., 178 (2002), 373-390.
[29] B. Engquist, A.-K. Tornberg and R. Tsai, Discretization of Dirac delta functions in level set methods, J. Comput. Phys., 207(1) (2005), 28-51.
[30] E. Fatemi, B. Engquist and S. J. Osher, Numerical solution of the high frequency asymptotic expansion for the scalar wave equation, J. Comput. Phys., 120(1) (1995), 145-155.
[31] S. Fomel and J. A. Sethian, Fast-phase space computation of multiple arrivals, Proc. Nat. Acad. Sci. USA, 99(11) (2002), 7329-7334 (electronic).
[32] S. Geoltrain and J. Brac, Can we image complex structures with first-arrival traveltime?, Geophysics, 58(4) (1993), 564-575.
[33] P. Gérard, Microlocal defect measures, Commun. Part. Diff. Eq., 16(11) (1991), 1761-1794.
[34] P. Gérard, P. A. Markowich, N. J. Mauser and F. Poupaud, Homogenization limits and Wigner transforms, Commun. Pur. Appl. Math., 50(4) (1997), 323-379.
[35] L. Gosse, Using K-branch entropy solutions for multivalued geometric optics computations, J. Comput. Phys., 180(1) (2002), 155-182.
[36] L. Gosse, S. Jin and X. Li, Two moment systems for computing multiphase semiclassical limits of the Schrödinger equation, Math. Mod. Meth. Appl. Sci., 13(12) (2003), 1689-1723.
[37] L. Gosse and O. Runborg, Finite moment problems and applications to multiphase computations in geometric optics, Commun. Math. Sci., 3 (2005), 373-392.
[38] L. Gosse and O. Runborg, Resolution of the finite Markov moment problem, C. R. Math. Acad. Sci. Paris, Ser I, 341 (2005), 775-780.
[39] H. Grad, On the kinetic theory of rarefied gases, Commun. Pur. Appl. Math., 2 (1949), 331-407.
[40] G. A. Hagedorn, Semiclassical quantum mechanics. I. The $\hbar \to 0$ limit for coherent states, Commun. Math. Phys., 71(1) (1980), 77-93.
[41] R. F. Harrington, Field Computation by Moment Methods, MacMillan, 1968.
[42] L. Hörmander, The Analysis of Linear Partial Differential Operators. I-IV, Springer-Verlag, Berlin, 1983-1985.
[43] U. Jakobus and F. M. Landstorfer, Improved PO-MM hybrid formulation for scattering from three-dimensional perfectly conducting bodies of arbitrary shape, IEEE T. Antennas Propag., 43(2) (1995), 162-169.
[44] S. Jin and X. Li, Multi-phase computations of the semiclassical limit of the Schrödinger equation and related problems: Whitham vs. Wigner, Physica D, 182(1-2) (2003), 46-85.

[45] S. Jin, H. Liu, S. Osher and R. Tsai, Computing multi-valued physical observables for the high frequency limit of symmetric hyperbolic systems, J. Comput. Phys., 210(2) (2005), 497-518.
[46] S. Jin, H. Liu, S. Osher and R. Tsai, Computing multivalued physical observables for the semiclassical limit of the Schrödinger equation, J. Comput. Phys., 205(1) (2005), 222-241.
[47] S. Jin and S. Osher, A level set method for the computation of multivalued solutions to quasi-linear hyperbolic PDEs and Hamilton-Jacobi equations, Commun. Math. Sci., 1(3) (2003), 575-591.
[48] S. Jin and X. Wen, Hamiltonian-preserving schemes for the Liouville equation with discontinuous potentials, Commun. Math. Sci., 3(3) (2005), 285-315.
[49] S. Jin and X. Wen, Hamiltonian-preserving schemes for the Liouville equation of geometrical optics with discontinuous local wave speeds, J. Comput. Phys., 214(2) (2006), 672-697.
[50] B. R. Julian and D. Gubbins, Three-dimensional seismic ray tracing, J. Geophys. Res., 43 (1977), 95-114.
[51] C. Y. Kao, S. Osher and J. Qian, Lax-Friedrichs sweeping scheme for static Hamilton-Jacobi equations, J. Comput. Phys., 196(1) (2004), 367-391.
[52] J. Keller, Geometrical theory of diffraction, J. Opt. Soc. Am., 52 (1962), 116-130.
[53] S. Kim, An $\mathcal{O}(N)$ level set method for eikonal equations, SIAM J. Sci. Comput., 22(6) (2000), 2178-2193.
[54] S. Kim and R. Cook, 3-D traveltime computation using second-order ENO scheme, Geophysics, 64(6) (1999), 1867-1876.
[55] R. G. Kouyoumjian and P. H. Pathak, A uniform theory of diffraction for an edge in a perfectly conducting surface, Proc. IEEE, 62(11) (1974), 1448-1461.
[56] Y. A. Kravtsov, On a modification of the geometrical optics method, Izv. VUZ Radiofiz., 7(4) (1964), 664-673.
[57] G. Lambaré, P. S. Lucio and A. Hanyga, Two-dimensional multivalued traveltime and amplitude maps by uniform sampling of ray field, Geophys. J. Int., 125 (1996), 584-598.
[58] R. T. Langan, I. Lerche and R. T. Cutler, Tracing of rays through heterogeneous media: An accurate and efficient procedure, Geophysics, 50 (1985), 1456-1465.
[59] S. Langdon and S. N. Chandler-Wilde, A wavenumber independent boundary element method for an acoustic scattering problem, SIAM J. Numer. Anal., 43 (2006), 2450-2477.
[60] C. D. Levermore, Moment closure hierarchies for kinetic theories, J. Stat. Phys., 83(5-6) (1996), 1021-1065.
[61] B. R. Levy and J. Keller, Diffraction by a smooth object, Commun. Pur. Appl. Math., 12 (1959), 159-209.
[62] H. Ling, R. Chou and S. W. Lee, Shooting and bouncing rays: Calculating the RCS of an arbitrarily shaped cavity, IEEE T. Antenn. Propag., 37 (1989), 194-205.
[63] P.-L. Lions and T. Paul, Sur les mesures de Wigner, Rev. Mat. Iberoam., 9(3) (1993), 553-618.
[64] H. Liu, L.-T. Cheng, and S. Osher, A level set framework for capturing multi-valued solutions of nonlinear first-order equations, J. Sci. Comput., 29(3) (2006), 353-373.
[65] H. Liu, S. Osher and R. Tsai, Multi-valued solution and level set methods in computational high frequency wave propagation, Commun. Comput. Phys., 1(5) (2006), 765-804.
[66] D. Ludwig, Uniform asymptotic expansions at a caustic, Commun. Pur. Appl. Math., 19 (1966), 215-250.
[67] V. P. Maslov, Théorie des Perturbations et Méthodes Asymptotiques, Izd. Moskov. Univ., 1965 (in Russian); Dunod, Paris, 1972 (French translation).
[68] L. N. Medgyesi-Mitschang and D.-S. Wang, Hybrid methods for analysis of complex scat-

terers, P. IEEE, 77(5) (1989), 770-779.
[69] R. B. Melrose and M. E. Taylor, Near peak scattering and the corrected Kirchhoff approximation for a convex obstacle, Adv. Math., 55 (1985), 242-315.
[70] L. Miller, Refraction of high-frequency waves density by sharp interfaces and semiclassical measures at the boundary, J. Math. Pure. Appl. (9), 79(3) (2000), 227-269.
[71] M. Motamed and O. Runborg, A fast phase space method for computing creeping rays, J. Comput. Phys, 219(1) (2006), 276-295.
[72] S. J. Osher, L.-T. Cheng, M. Kang, H. Shim and Y.-H. Tsai, Geometric optics in a phase-space-based level set and Eulerian framework, J. Comput. Phys., 179(2) (2002), 622-648.
[73] S. J. Osher and R. P. Fedkiw, Level Set Methods and Dynamic Implicit Surfaces, Springer Verlag, 2002.
[74] S. J. Osher and J. A. Sethian, Fronts propagating with curvature-dependent speed: algorithms based on Hamilton-Jacobi formulations, J. Comput. Phys., 79(1) (1988), 12-49.
[75] S. J. Osher and C.-W. Shu, High-order essentially nonoscillatory schemes for Hamilton-Jacobi equations, SIAM J. Numer. Anal., 28(4) (1991), 907-922.
[76] V. Pereyra, W. H. K. Lee and H. B. Keller, Solving two-point seismic ray-tracing problems in a heterogeneous medium, B. Seismol. Soc. Am., 70 (1980), 79-99.
[77] J. Qian, L.-T. Cheng and S. Osher, A level set-based Eulerian approach for anisotropic wave propagation, Wave Motion, 37(4) (2003), 365-379.
[78] F. Qin, Y. Luo, K. B. Olsen, W. Cai and G. T. Schuster, Finite-difference solution of the eikonal equation along expanding wavefronts, Geophysics, 57(3) (1992), 478-487.
[79] J. Ralston, Gaussian beams and the propagation of singularities, in: Studies in Partial Differential Equations, MAA Stud. Math., vol. 23, Math. Assoc. America, Washington, DC, 1982, pp. 206-248.
[80] O. Runborg, Multiscale and multiphase methods for wave propagation, PhD thesis, NADA, KTH, Stockholm, 1998.
[81] O. Runborg, Some new results in multiphase geometrical optics, M2AN Math. Model. Numer. Anal., 34 (2000), 1203-1231.
[82] L. Ryzhik, G. Papanicolaou and J. B. Keller, Transport equations for elastic and other waves in random media, Wave Motion, 24(4) (1996), 327-370.
[83] J. A. Sethian, A fast marching level set method for monotonically advancing fronts, Proc. Nat. Acad. Sci. USA, 93(4) (1996), 1591-1595.
[84] J. A. Sethian, Level set methods and fast marching methods, in: Evolving Interfaces in Computational Geometry, Fluid Mechanics, Computer Vision, and Materials Science, Cambridge University Press, Cambridge, 2nd ed., 1999.
[85] P. Smereka, The numerical approximation of a delta function with application to level set methods, J. Comput. Phys., 211(1) (2006), 77-90.
[86] I. Solliec, Calcul optique multivalué et calcul d'energie électromagnétique en présence d'une caustique de type pli, PhD thesis, Université Pierre et Marie Curie, Paris 6, Paris, France, 2003.
[87] C. Sparber, N. Mauser and P. A. Markowich, Wigner functions vs. WKB-techniques in multivalued geometrical optics, J. Asympt. Anal., 33(2) (2003), 153-187.
[88] Y. Sun, Computation of 2D multiple arrival traveltime fields by an interpolative shooting method, in: Soc. Expl. Geophys., Extended Abstracts, 1992, pp. 1320-1323.
[89] W. W. Symes, A slowness matching finite difference method for traveltimes beyond transmission caustics, Preprint, Dept. of Computational and Applied Mathematics, Rice University, 1996.

[90] W. W. Symes and J. Qian, A slowness matching Eulerian method for multivalued solutions of eikonal equations, J. Sci. Comput., 19(1-3) (2003), 501-526.
[91] L. Tartar, H-measures, a new approach for studying homogenisation, oscillations and concentration effects in partial differential equations, Proc. Roy. Soc. Edinburgh Sect. A, 115(3-4) (1990), 193-230.
[92] G. A. Thiele and T. H. Newhouse, A hybrid technique for combining moment methods with a geometrical theory of diffraction, IEEE T. Antenn. Propag., 23 (1975), 62-69.
[93] R. Thom, Stabilité Structurelle et Morphogénèse, W. A. Benjamin, Inc., Reading, Maasachusets, 1972.
[94] C. H. Thurber and W. L. Ellsworth, Rapid solution of ray tracing problems in hetereogeneous media, B. Seismol. Soc. Am., 70 (1980), 1137-1148.
[95] A.-K. Tornberg, Interface tracking methods with applications to multiphase flows, PhD thesis, NADA, KTH, Stockholm, 2000.
[96] A.-K. Tornberg and B. Engquist, Interface tracking in multiphase flows, in: Multifield Problems, Springer, Berlin, 2000, pp. 58-65.
[97] A.-K. Tornberg and B. Engquist, The segment projection method for interface tracking, Commun. Pur. Appl. Math., 56(1) (2003), 47-79.
[98] A.-K. Tornberg and B. Engquist, Numerical approximations of singular source terms in differential equations, J. Comput. Phys., 200(2) (2004), 462-488.
[99] J. Towers, Two methods for discretizing a delta function on a level set, J. Comput. Phys., 220(2) (2007), 915-931.
[100] Y. R. Tsai, L. T. Cheng, S. Osher and H. K. Zhao, Fast sweeping algorithms for a class of Hamilton-Jacobi equations, SIAM J. Numer. Anal., 41(2) (2003), 673-694 (electronic).
[101] J. N. Tsitsiklis, Efficient algorithms for globally optimal trajectories, IEEE T. Automat. Contr., 40(9) (1995), 1528-1538.
[102] J. van Trier and W. W. Symes, Upwind finite-difference calculation of traveltimes, Geophysics, 56(6) (1991), 812-821.
[103] J. Vidale, Finite-difference calculation of traveltimes, B. Seismol. Soc. Am., 78(6) (1988), 2062-2076.
[104] V. Vinje, E. Iversen and H. Gjøystdal, Traveltime and amplitude estimation using wavefront construction, in: Eur. Ass. Expl. Geophys., Extended Abstracts, 1992, pp. 504-505.
[105] V. Vinje, E. Iversen and H. Gjøystdal, Traveltime and amplitude estimation using wavefront construction, Geophysics, 58(8) (1993), 1157-1166.
[106] G. B. Whitham, Linear and Nonlinear Waves, John Wiley & Sons, 1974.
[107] L. Yatziv, A. Bartesaghi and G. Sapiro, $\mathcal{O}(N)$ implementation of the fast marching algorithm, J. Comput. Phys., 212(2) (2006), 393-399.
[108] L. Ying and E. Candès, Fast geodesics computation with the phase flow method, J. Comput. Phys., 220(1) (2006), 6-18.
[109] L. Ying and E. Candès, The phase flow method, J. Comput. Phys., 220(1) (2006), 184-215.